ACS NANO
Cite This: ACS Nano 2019, 13, 7627−7643
www.acsnano.org

ARTICLE

Microphysiological Engineering of Self-Assembled and Perfusable Microvascular Beds for the Production of Vascularized Three-Dimensional Human Microtissues

Jungwook Paek,[†,○] Sunghee E. Park,[†,○] Qiaozhi Lu,[†] Kyu-Tae Park,[†] Minseon Cho,[†] Jeong Min Oh,[†] Keon Woo Kwon,[†] Yoon-suk Yi,[†] Joseph W. Song,[†] Hailey I. Edelstein,[‡] Jeff Ishibashi,[§,∥] Wenli Yang,[‡] Jacob W. Myerson,[⊥] Raisa Y. Kiseleva,[⊥] Pavel Aprelev,[⊥] Elizabeth D. Hood,[⊥] Dwight Stambolian,[#] Patrick Seale,[§,∥] Vladimir R. Muzykantov,[⊥] and Dongeun Huh*[,†,‡,▽]

[†]Department of Bioengineering, [‡]Institute for Regenerative Medicine, [§]Institute for Diabetes, Obesity and Metabolism (IDOM), [∥]Department of Cell and Developmental Biology, [⊥]Department of Systems Pharmacology and Translational Therapeutics and Center for Translational Targeted Therapeutics and Nanomedicine, and [#]Department of Ophthalmology, Perelman School of Medicine, and [▽]NSF Science and Technology Center for Engineering Mechanobiology, University of Pennsylvania, Philadelphia, Pennsylvania 19104, United States

Supporting Information

ABSTRACT: The vasculature is an essential component of the circulatory system that plays a vital role in the development, homeostasis, and disease of various organs in the human body. The ability to emulate the architecture and transport function of blood vessels in the integrated context of their associated organs represents an important requirement for studying a wide range of physiological processes. Traditional *in vitro* models of the vasculature, however, largely fail to offer such capabilities. Here we combine microfluidic three-dimensional (3D) cell culture with the principle of vasculogenic self-assembly to engineer perfusable 3D microvascular beds *in vitro*. Our system is created in a micropatterned hydrogel construct housed in an elastomeric microdevice that enables coculture of primary human vascular endothelial cells and fibroblasts to achieve *de novo* formation, anastomosis, and controlled perfusion of 3D vascular networks. An open-top chamber design adopted in this hybrid platform also makes it possible to integrate the microengineered 3D vasculature with other cell types to recapitulate organ-specific cellular heterogeneity and structural organization of vascularized human tissues. Using these capabilities, we developed stem cell-derived microphysiological models of vascularized human adipose tissue and the blood−retinal barrier. Our approach was also leveraged to construct a 3D organotypic model of vascularized human lung adenocarcinoma as a high-content drug screening platform to simulate intravascular delivery, tumor-killing effects, and vascular toxicity of a clinical chemotherapeutic agent. Furthermore, we demonstrated the potential of our platform for applications in nanomedicine by creating microengineered models of vascular inflammation to evaluate a nanoengineered drug delivery system based on active targeting liposomal nanocarriers. These results represent a significant improvement in our ability to model the complexity of native human tissues and may provide a basis for developing predictive preclinical models for biopharmaceutical applications.

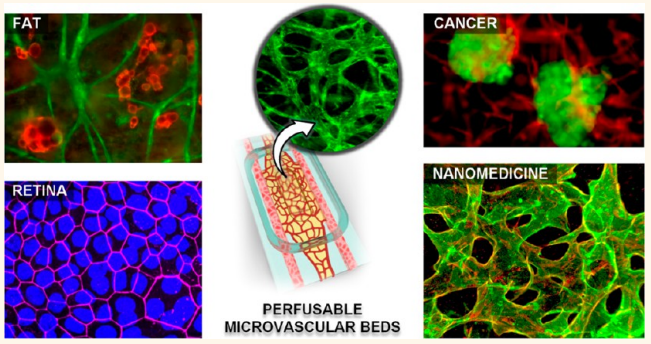

KEYWORDS: *organ-on-a-chip, vasculature, 3D culture, nanomedicine, cancer, adipose, retina*

Vascularity is an essential anatomical feature of virtually every organ in the human body. By providing a conduit for hemodynamic flow, blood vessels constitute the main component of the circulatory system indispensable to the development and homeostasis of various organ systems.[1] In particular, the vasculature is responsible for

Received: January 25, 2019
Accepted: June 13, 2019
Published: June 13, 2019

DOI: 10.1021/acsnano.9b00686
ACS Nano 2019, 13, 7627−7643

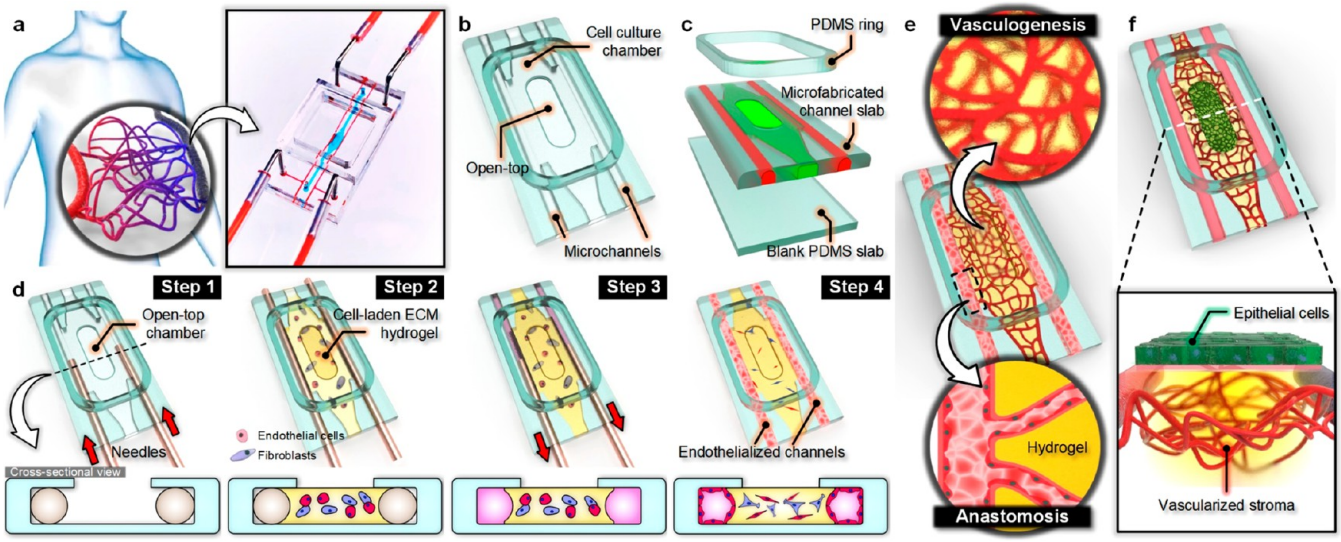

Figure 1. A microengineered *in vitro* 3D culture platform to produce self-assembled and perfusable microvascular beds. a. Our microengineered cell culture device is used to engineer *in vivo*-like 3D networks of blood vessels. b. The device consists of a cell culture chamber with a top opening and two parallel microchannels used for controlled vascular perfusion. c. This multilayered device is fabricated by sealing microfabricated channels against a blank PDMS slab and bonding a PDMS ring used as a medium reservoir. d. To form the vasculature, template needles are inserted into the microchannels (Step 1), and this step is followed by the injection of endothelial cells and fibroblasts suspended in an ECM hydrogel solution into the cell culture chamber (Step 2). Once gelation is complete, the needles are pulled out to generate hollow microchannels (Step 3), which are then seeded with vascular endothelial cells to create endothelialized and externally accessible compartments on both sides of the cell-laden scaffold (Step 4). e. During cell culture, the endothelial cells in the hydrogel undergo vasculogenesis and self-assemble into interconnected endothelial tubes that together form a 3D multicellular structure reminiscent of microvascular plexus *in vivo*. The vessels in the hydrogel also anastomose with the endothelium in the side channels to form a perfusable network. f. The open top of the cell culture chamber can be used for culturing another cell type, such as epithelial cells, directly on the surface of the vessel-containing ECM hydrogel scaffold to mimic the structural organization of vascularized 3D tissues in a more realistic manner.

mediating the exchange of gases, nutrients, metabolites, immune components, hormones, and other biomolecules between the blood and perfused tissues during diverse physiological processes.[2−5] Studies have also shown that vascular complications due to abnormal changes in the architecture, biological phenotype, and hemodynamic environment of blood vessels are associated with a wide variety of pathological conditions including diabetes,[6] obesity,[7] hypertension,[8] age-related macular degeneration,[9] and cancer.[10] Therefore, the ability to model and examine the structure and function of the vasculature is of critical importance in investigating the physiology of vascularized tissues and organs in the human body.

Over the past few decades, the significant need for such capabilities has stimulated considerable research efforts to develop physiologically relevant *in vitro* models of the vasculature. Many of these early studies focused on incorporating perfusable cell culture chambers to simulate the dynamic flow environment of blood vessels.[11,12] By recapitulating flow-generated physiological mechanical cues not captured in static culture, these model systems have proven instrumental in advancing our fundamental understanding of vascular endothelial cells.[11,12] With the increasing attention to the multiscale nature of physiological and disease processes in the vascular system,[13] there is now a rapidly growing need to expand the scope of research beyond the cellular level to investigate integrated vascular structure and function at the tissue and organ levels. Despite significant advances, however, existing *in vitro* vascular models are greatly limited in their ability to meet this important need. Two-dimensional (2D) monolayers of endothelial cells often used in these systems fail to represent the higher-level architecture of the *in vivo* vasculature characterized by complex three-dimensional (3D) networks of interconnected and perfusable endothelial tubes.[14] This limitation is particularly problematic in modeling small blood vessels in the microcirculatory system that play an essential role in the regulation of tissue perfusion.[15,16] Conventional approaches, most of which are based on monoculture of endothelial cells, also present major challenges to reconstituting the structural and functional integration of the vasculature with other cell types in an organ-specific manner.[17] To address these important drawbacks of traditional vascular models, advanced techniques are needed to more faithfully recapitulate the native complexity of the vasculature in an integrated physiological context.

Here we demonstrate the feasibility of engineering an *in vitro* platform to transform primary culture of human endothelial cells into microphysiological models of blood vessels. Our approach builds upon advanced *in vitro* techniques derived from recent progress in the development of microengineered perfusable blood vessels[18−27] and hydrogel-based microphysiological systems[14,28,29] to combine microfluidic 3D cell culture with the principle of vasculogenesis, a critical developmental process by which new blood vessels are formed *de novo*.[30] Specifically, we used a template-assisted fabrication technique to build a hybrid microfluidic platform that contains perfusable microchannels in an extracellular matrix (ECM) hydrogel scaffold housed in a multilayered elastomeric device. This system was used for primary culture of human vascular endothelial cells and fibroblasts to emulate the process of vasculogenesis and to induce spontaneous formation of perfusable 3D vascular networks distributed throughout the

DOI: 10.1021/acsnano.9b00686
ACS Nano 2019, 13, 7627−7643

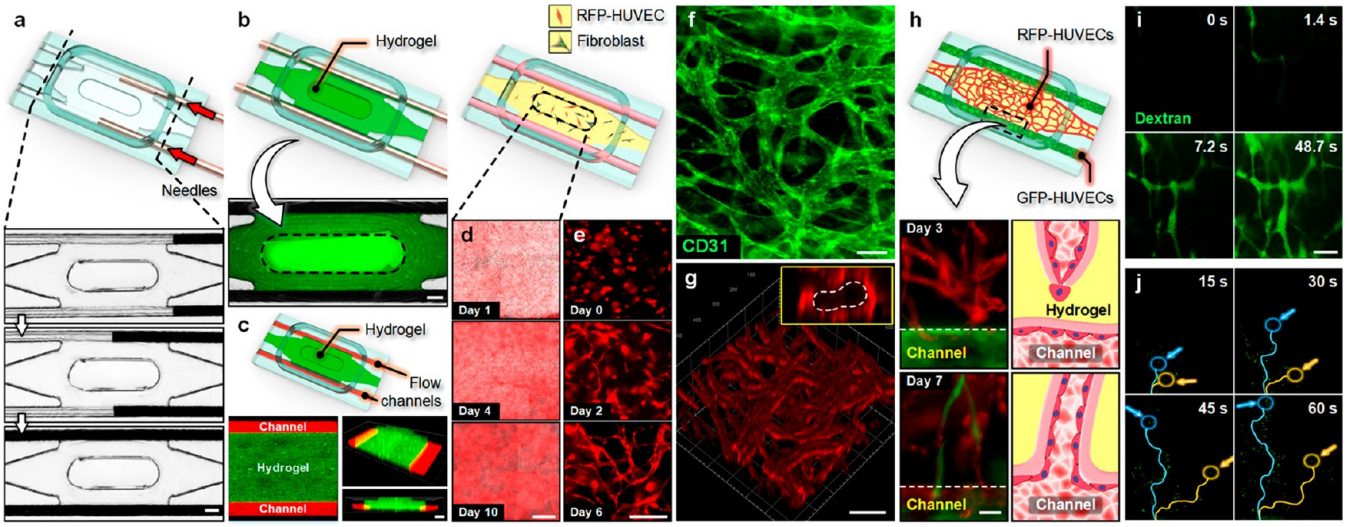

Figure 2. Microfluidic tissue engineering of perfusable 3D microvessels. a. Production of blood vessels in our model begins with the insertion of thin needles (shown as dark objects) guided by the side microchannels. Scale bar, 400 μm. b. With the needles in place, the culture chamber is filled with a fibrinogen solution mixed with thrombin. The 1-μm microbeads fluorescently labeled green were added to the matrix solution for visualization purposes. Scale bar, 400 μm. c. The side channels created by removing the needles from the solidified fibrin scaffold are injected with 1-μm red fluorescent beads. Scale bar, 200 μm. d, e. Over time, coculture of RFP-HUVECs (red) and human lung fibroblasts (not shown) in the hydrogel leads to the formation of network structures. Scale bars, (d) 250 μm and (e) 200 μm. f. Immunofluorescence staining of CD31 expressed by the endothelial tubes in the self-assembled vascular network. Scale bar, 100 μm. g. 3D confocal rendering of 3D vessels distributed throughout a 400 μm-thick hydrogel construct. The inset shows a cross-section of a vessel with an open lumen (white dotted line). Scale bar, 200 μm. h. The physical interaction between the self-assembled vessels (red) and the endothelial lining of the side channels (green) is visible at the hydrogel−channel interface (white dotted line). Scale bar, 100 μm. After anastomosis, the engineered vessels become perfusable as visualized by the flow of (i) 70 kDa FITC−dextran (scale bar, 200 μm) and (j) 1-μm fluorescent beads. The blue and yellow lines in j show the trajectories of two fluorescent particles flowing through the vasculature (see Supplementary Movie 1).

scaffold. Importantly, we implemented an open-top design in this cell culture system to enable integration of the microengineered vasculature with other types of specialized tissue. We demonstrate this capability by presenting stem cell-based microphysiological models of vascularized human adipose tissue and the interface between the retina and the choroidal blood vessels. Moreover, we show that tumor spheroids can be incorporated into our engineered microvascular beds to construct an *in vitro* model of vascularized adenocarcinoma in the human lung. We demonstrate the feasibility of using this disease model as a high-content drug screening platform by simulating the efficacy and vascular toxicity of a chemotherapeutic drug in current clinical use for advanced lung cancer. Finally, we present microengineered models of vascular inflammation for *in vitro* evaluation of nanoengineered liposomes designed for targeted intravascular drug delivery.

MODEL DESIGN AND CONSTRUCTION

Our microphysiological model is constructed in an elastomeric cell culture device made out of poly(dimethylsiloxane) (PDMS) that consists of multiple compartments necessary for *in vitro* tissue engineering and controlled perfusion of 3D microvascular networks (Figure 1a). The microengineered device consists of a cell culture chamber which is open to an upper medium reservoir and flanked by two parallel microchannels (Figure 1b). To make this device, a PDMS layer containing microfabricated channel features with a large opening is bonded to a rectangular PDMS ring and a blank slab of PDMS (Figure 1c). In the first step of establishing cell culture in this device, a long needle is inserted into each microchannel through the inlet access ports oriented sideways (Figure 1d, step 1). Subsequently, an ECM hydrogel precursor solution mixed with a suspension of primary human vascular endothelial cells and fibroblasts is injected into the cell culture chamber and enzymatically solidified to form a cell-laden hydrogel scaffold (Figure 1d, step 2). After gelation, the needles are gently removed from the microchannels to create hollow circular channels (Figure 1d, step 3), which are then seeded with vascular endothelial cells to form an endothelium on the luminal surface (Figure 1d, step 4).

During culture, the endothelial cells dispersed throughout the ECM scaffold spread, proliferate, interconnect, and self-assemble into a network of microvessels with open lumens, approximating vasculogenesis during embryonic development and adult vascular growth *in vivo* (Figure 1e). The fibroblasts in the hydrogel play an essential role in this process by producing soluble factors and matrix proteins that have been shown to promote lumen formation and the stability of microvascular structures.[31] Another critical step in the construction of our model is to establish physical connection between the vascular network formed in the hydrogel scaffold and the flow channels on the sides. This is accomplished by vascular anastomosis that occurs spontaneously *via* fusion of the microvascular tubes in the hydrogel scaffold with the endothelial lining of the side microchannels (Figure 1e).[32] Completion of this process provides a means to interface the microengineered vasculature with the external world and to generate pressure gradient across the hydrogel scaffold to perfuse the vascular network in a controlled manner.

Our platform also makes it possible to incorporate other types of cells into the perfusable microvascular beds to model various kinds of vascularized human tissues. For example, the

DOI: 10.1021/acsnano.9b00686
ACS Nano 2019, 13, 7627−7643

opening of the cell culture chamber can be used to grow epithelial cells directly on the surface of the hydrogel scaffold and to form a multilayered tissue unit that resembles the mucosa and its underlying vascularized stroma or other epithelial-endothelial interfaces responsible for key physiological processes such as barrier function (Figure 1f). It is also possible to embed cells with specialized functions in the ECM scaffold along with endothelial cells and fibroblasts to mimic vascularized parenchymal tissues. In this case, the opening of the chamber provides a means to increase media supply and facilitate diffusive transport of nutrients, oxygen, and soluble factors into the hydrogel to support cell growth and differentiation prior to the formation of perfusable vasculature. Importantly, these approaches can be implemented in an organ-specific manner by using cells derived from the same organ. In any case, the open-top design of our system provides easy access to the cultured tissues and facilitates the process of engineering the multicellular complexity and microenvironment of these models.

RESULTS/DISCUSSION

Engineering of 3D Vascular Networks in Perfusable ECM Hydrogel Scaffolds. Our study first focused on demonstrating the method of using needle templates to generate perfusable hydrogel cell culture scaffolds. When the needles were inserted into the access ports, the two parallel microchannels physically guided them to slide along the entire length of our device without noticeable deflection (Figure 2a). The fibrinogen solution injected in the subsequent step advanced along the cell culture compartment without moving the inserted needles and filled the entire chamber within a minute (Figure 2b). During this process, we did not observe any spillage of the solution through the open top of the chamber presumably because the meniscus of the solution was pinned at the edge of the opening due to surface tension. Following gelation for 15 min, the needle templates were removed from the fibrin scaffold to generate flow channels on both sides of the hydrogel construct in the culture chamber (Figure 2c). When we introduced a cell culture medium into the side microchannels and the medium reservoir to hydrate the device, the micropatterned scaffold remained stable without showing significant structural changes.

Our microengineered system containing this fibrin scaffold was then used as a coculture platform to produce 3D vascular networks. To demonstrate the proof-of-principle of this approach, we created a model system using red fluorescent protein (RFP)-expressing human umbilical vein endothelial cells (HUVECs) and human lung fibroblasts as representative cell populations. After hydrogel loading, the cells were uniformly dispersed throughout the gel and began to spread within 24 h of seeding. During culture, the embedded cells were observed to undergo active proliferation as illustrated by a continuous increase in the intensity of RFP in the cell culture chamber (Figure 2d). The increasing cell number, however, had negligible effects on the structural integrity of the scaffold, and the cell-laden hydrogel construct remained stable and firmly attached to the surface of the chamber for the entire duration of culture (>10 days). Importantly, microfluorimetric imaging of the cells revealed the development of network structures in the fibrin hydrogel (Figure 2e). As early as on day 2, HUVECs appeared significantly elongated and began to organize into chord-like structures (Day 2 in Figure 2e). These morphological changes became more pronounced over time and eventually led to the formation of cellular networks that resembled the primitive vascular plexus generated by vasculogenesis *in vivo* (Day 6 in Figure 2e). Immunostaining analysis also showed intricate networks of interconnected endothelial tubes with an average diameter of 24 ± 7.05 μm (mean ± SD) that exhibited robust expression of cluster of differentiation 31 (CD31) (Figure 2f).

It should be noted that our engineered microvessels were distributed throughout the hydrogel construct with a thickness of 400 μm (Figure 2g), which is significantly thicker than ECM scaffolds typically used in other microfluidic vascular models.[18−27] We speculate that the ability to vascularize thick tissues in our system is enabled mainly by the open-top design of the device that greatly increases the area of contact between the hydrogel scaffold and cell culture medium to improve the supply of nutrients and oxygen deep into the engineered 3D tissue constructs. This capability makes our platform attractive for recapitulating three-dimensionality of the native vasculature.

Perfusion of the Microengineered Vascular Networks. Next, we investigated the perfusability of our engineered vasculature. Since the microvessels were situated within the hydrogel scaffold, their intravascular space was not readily accessible from the external compartment, making it challenging to achieve vascular perfusion in our model. To address this issue, we cultured HUVECs in the side microchannels and allowed them to connect with the 3D vessels in the hydrogel through the process of vascular anastomosis.[32,33] In these experiments, HUVECs expressing green fluorescent protein (GFP) were seeded into the channels 1 day after hydrogel loading to visualize anastomosis. After seeding, GFP-HUVECs were continuously perfused with medium to form confluent monolayers within the first 2 days of culture, after which they began to migrate into the gel. The endothelial sprouts formed by this directional migration then appeared to establish connections with the nascent vessels assembled in the scaffold and integrate into the vascular network (Figure 2h). The same pattern of anastomosis was observed along the entire length of the interface between the cell culture chamber and the endothelialized side channels.

We then asked whether the anastomosed endothelium in the side channels provided fluidic access to the lumens of the engineered vessels in the hydrogel. To examine this question, we injected a fluorescently labeled solution containing 70 kDa FITC-dextran into one of the endothelialized microchannels and generated a pressure gradient across the vascularized hydrogel. Under this condition, the solution was observed to enter the microvessels and flow in the direction of applied pressure gradient, eventually reaching the microchannel on the other side of the cell culture chamber (Figure 2i). During flow, the dextran solution remained in the intravascular space without leaking into the surrounding scaffold, illustrating barrier integrity of the engineered vessels. We also conducted similar experiments using 1 μm fluorescent particles to show a continuous flow of the microbeads through the vascular network (Figure 2j; Supplementary Movie 1). These results clearly demonstrate the perfusability of the anastomosed 3D vasculature in our model. Given the small size of the engineered vessels, the data also suggest the possibility of using our system to simulate microvascular perfusion in a physiologically relevant 3D environment.

Microphysiological Model of Vascularized Human Adipose Tissue. In the next phase of our study, we set out to

DOI: 10.1021/acsnano.9b00686
ACS Nano 2019, 13, 7627−7643

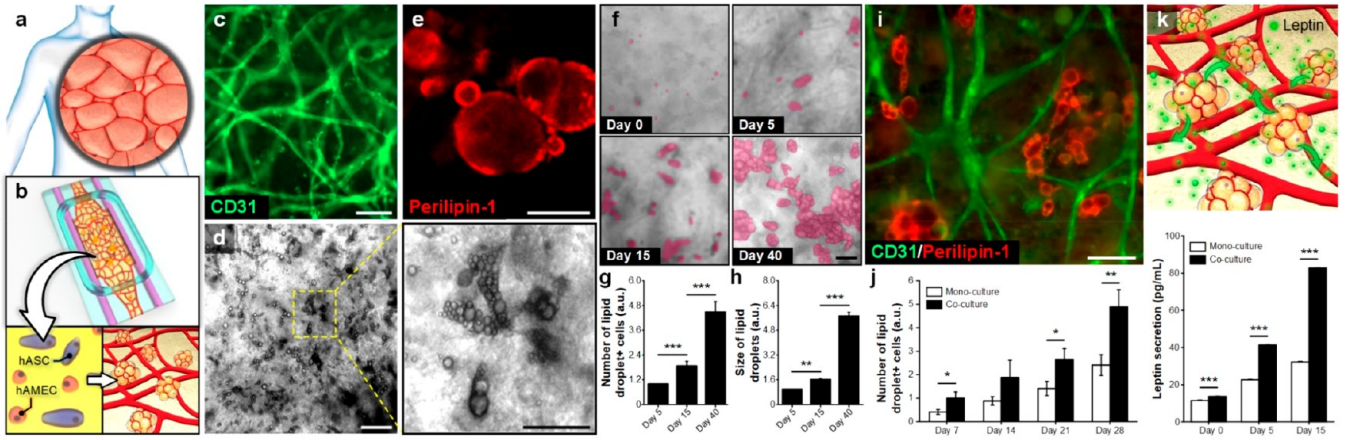

Figure 3. Construction of vascularized human adipose tissue *in vitro*. a, b. The highly vascularized human white adipose tissue is recreated in our model by coculturing hASCs and hAMECs in a fibrin hydrogel scaffold to induce adipogenesis and vasculogenesis simultaneously. c. Over a period of 2 weeks, hAMECs organize themselves into a 3D vascular network visualized by immunostaining of CD31. Scale bar, 100 μm. d. Concurrently, hASCs differentiate into adipocytes recognized by their intracellular lipid droplets visible in phase contrast micrographs taken on day 40. Scale bar, 100 μm (scale bar for magnified micrograph, 50 μm). e. Adipogenic differentiation of hASCs is further evidenced by their expression of perilipin-1 after 40 days of culture. Scale bar, 100 μm. f, g. As culture progresses, the number of lipid droplet-containing cells increases. Scale bar, 100 μm. h. The size of lipid droplets in the differentiated cells also increase with time. i. A micrograph of vascularized adipose tissue construct after 40-day culture in our device. Scale bar, 100 μm. j. Adipogenic differentiation occurs more rapidly in the coculture of hAMECs and hASCs as compared with the hASC monoculture model. k. ELISA analysis of conditioned media collected from our engineered adipose tissue reveals increased leptin production due to the vasculature. The results in j and k indicate the significant contribution of endothelial cells to adipogenic differentiation of hASCs. Data are presented as mean ± SEM. $^{**}P < 0.01$ and $^{***}P < 0.001$ ($n = 3$).

leverage the demonstrated capabilities of our platform to develop specialized *in vitro* models that combined the engineered vasculature with other types of cells to emulate vascularized human tissues. To this end, we chose adipose tissue as a model system and explored the feasibility of using our microdevice to mimic human subcutaneous white adipose tissue (WAT) (Figure 3a). As the major site of energy storage in the body, WAT is mostly composed of adipocytes that store and release lipids in accordance with systemic energy levels and also secrete a variety of hormones to regulate metabolism.[34] Conventionally, the study of WAT has relied predominantly on the monolayer culture of adipocytes. This traditional approach, however, has been shown to prevent adipocytes from assuming their physiological 3D morphology and to induce the expression of fibrotic and inflammatory phenotypes.[35] The conventional models are also greatly limited in their ability to recapitulate structural and functional coupling of adipocytes with other cell types that play a critical role in the physiological function of WAT. In particular, WAT is highly vascularized and relies on vascular transport of nutrients, oxygen, cells, and various soluble factors to maintain tissue homeostasis and to carry out its specialized functions.[36] Studies have also shown that the development and repair of WAT occur in coordination with the vasculature.[37,38] Despite the increasing recognition of the vasculature as a critical component of WAT, modeling this essential feature using traditional *in vitro* techniques remains a significant challenge.

To suggest an alternative *in vitro* strategy to tackle this problem, we focused on using the microengineered vascular platform to model the vascularized architecture of human WAT. In this study, we embedded human adipose-derived stem cells (hASCs) and primary human adipose microvascular endothelial cells (hAMECs) isolated from WAT in a hydrogel scaffold composed of type I collagen and fibrin and cocultured them for extended periods (over 40 days) to induce adipogenesis and vasculogenesis simultaneously (Figure 3b). We included collagen in the hydrogel due to its promotive effects on adipogenesis[39−41] and also engineered the scaffold by adjusting ECM concentrations and ratios to achieve the level of stiffness that has been shown to support adipogenic differentiation of stem cells (Figure S2).[42−44] The 3D coculture configuration was based on previous reports that adipose-derived stem cells have the capacity to produce soluble factors to trigger and support the formation of the vasculature in adipose tissue.[45] Consistent with these results, hAMECs grown in our model underwent robust vasculogenesis in the presence of hASCs and formed a 3D network of interconnected endothelial tubes throughout the hydrogel scaffold (Figure 3c). Interestingly, the generated vessels appeared to be smaller yet more organized and denser than those created by HUVECs (Figure S3), illustrating the microvascular origin of hAMECs. In comparison to HUVECs, the hAMECs were also assembled into 3D vessels more slowly but the resultant vasculature remained stable and maintained its network structure during prolonged culture (over 40 days). Considering that similar differences occur in traditional 3D culture models (data not shown), these results are not specific to the microfluidic culture environment, but they highlight the significant effect of endothelial phenotype on vascular development.

In concurrence with this process of vasculogenesis, the hASCs embedded in the same scaffold began to differentiate into adipocytes. Phase contrast imaging of the construct showed clusters of cells throughout the gel that contained large, spherical organelles (Figure 3d). These intracellular structures were stained positive with perilipin-1, which is a specific marker of lipid droplets,[46,47] indicating the differentiation of hASCs into adipocytes (Figure 3e). The number of these cells and the size of their lipid droplets increased with time, and the differentiated adipocytes were clearly visible

DOI: 10.1021/acsnano.9b00686
ACS Nano 2019, 13, 7627−7643

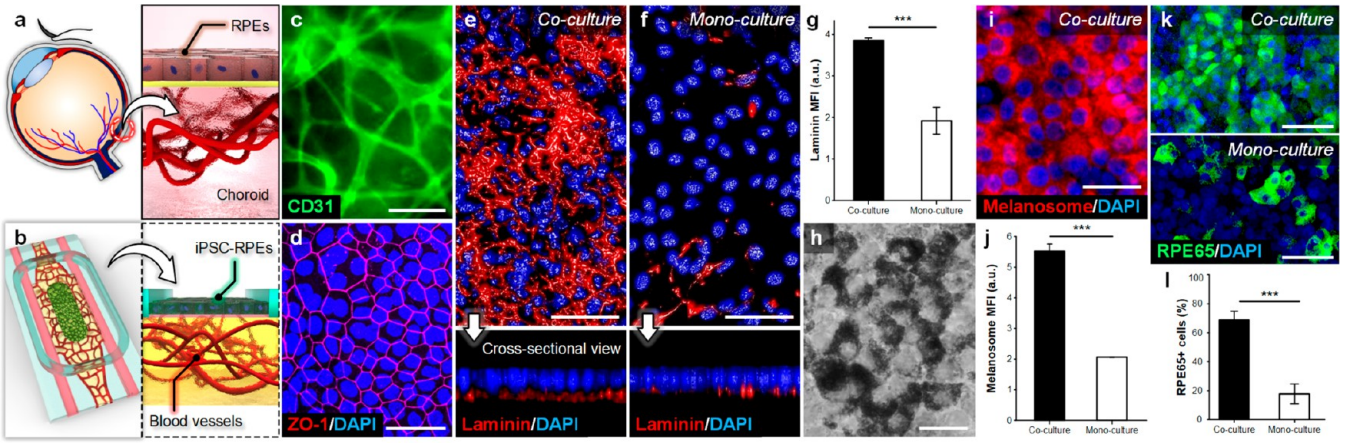

Figure 4. Microengineered model of the blood−retinal barrier. a. The blood−retinal barrier is formed by a monolayer of RPEs and the choroidal capillary bed in the outer layers of the retina in the human eye. b. This multilayered tissue−tissue interface is modeled in our device by culturing human iPSC-derived RPEs on the surface of a hydrogel construct containing a network of blood vessels. c. CD31 staining of microvessels constructed by primary human retinal microvascular endothelial in coculture with choroidal fibroblasts embedded in a fibrin scaffold. The image was taken on day 14. Scale bar, 50 μm. d. The iPSC-derived RPEs proliferate and form a confluent monolayer that expresses well-defined intercellular tight junctions (ZO-1) after 14 days of culture. Scale bar, 50 μm. e−g. Production of basement membrane proteins by RPEs is visualized by immunostaining of laminin (red) accumulated on the basolateral side of the epithelium. Analysis of immunofluorescence after 14 days of culture shows substantially increased laminin deposition in coculture of RPEs and vessels. Scale bar, 50 μm. h. Prolonged culture (14 days) in our model also leads to the pigmentation of RPEs as evident from the formation of dark granules in the RPEs shown by bright-field microscopy. Scale bar, 20 μm. i. The pigmented RPEs show robust expression of melanosomes in the cytoplasmic compartment. Scale bar, 25 μm. j. The number of melanosome-expressing RPEs increases significantly due to the presence of choroidal vessels in the hydrogel scaffold. k, l. The beneficial effect of the engineered blood vessels is further demonstrated by the increased expression of RPE-specific marker (RPE65) in the coculture (14 days) model. Scale bar, 50 μm. Data are presented as mean ± SEM. ***$P < 0.001$ ($n = 3$).

throughout the entire scaffold after 30 days of culture (Figure 3f−h). Of note is that when the hASCs were grown in a closed cell culture chamber using the same media and scaffold, the number of differentiated adipocytes was greatly reduced for the same duration of culture (14 days) (Figure S4). We suspect that this difference is due to the increased supply of nutrients and adipogenic factors to the hASCs through the opening of the culture chamber. As demonstrated in Figure 3i, 40-day culture in our system produced highly vascularized 3D tissue constructs interspersed with a large number of adipocytes. During prolonged culture over 40 days, the lipid droplets continued to increase in size and number, forming densely packed tissue constructs (Figure S5).

Importantly, these results also led us to ask whether our engineered microvasculature had any significant effects on hASC differentiation in our model. Blood vessels in adipose tissue have been suggested as the key component of an adipogenic niche that provides supporting signals for adipocyte development *in vivo*.[38,45,48] Inspired by these studies, we compared adipocyte differentiation and maturation in our vascularized model to those in a monoculture of hASCs established in the same microdevice. First, we examined the difference in the rate of adipogenic differentiation by comparing the numbers of cells with lipid droplets over time. As shown in Figure 3j, the differentiation of hASCs into adipocytes occurred regardless of the vasculature, but the vascularized models exhibited a substantially higher rate of differentiation, yielding nearly twice as many lipid droplet-containing cells as a monoculture of hASCs over 28 days. We also measured the production of leptin, which is one of the most important adipokines secreted by mature adipocytes to regulate energy balance and insulin sensitivity.[49,50] Our enzyme-linked immunosorbent assay (ELISA) analysis of conditioned media collected from our devices yielded measurable amounts of leptin in both models. The level of leptin in the vascularized construct, however, was found to be significantly higher than that measured in the monoculture device. For instance, coculture of hASCs with hAMECs for 15 days resulted in a more than 2-fold increase in the concentration of leptin as compared to a monoculture of hASCs (Figure 3k). Our results also showed increasing leptin concentrations over time in both cases, but this trend occurred in a more accelerated manner in the vascularized construct (Figure 3k). While further characterization is necessary, these data demonstrate that the tissue-specific vasculature engineered in our system allows for more efficient and rapid differentiation of hASCs into adipocytes, providing strong justification for inclusion of vascular components in modeling adipose tissue *in vitro*. These types of vascularized models may provide a research platform to simulate and mechanistically investigate various physiological and pathophysiological processes in human adipose tissue.

Microengineering of the Blood−Retinal Barrier. The open-top design of the cell culture chamber in our system provides a means not only to increase medium supply to the cells cultured in the hydrogel scaffold but also to form planar tissue layers directly on the surface of the engineered vascular constructs to mimic the interface between blood vessels and parenchymal tissues in an organ-specific manner. To demonstrate this capability, we developed a microphysiological system designed to reconstruct the barrier between the retinal pigment epithelium and the microvasculature in the outer layers of the retina in the human eye. This tissue−tissue interface, termed the outer blood−retinal barrier (oBRB), is formed by tight junctions between retinal pigment epithelial cells (RPEs) anchored to a specialized basement membrane

DOI: 10.1021/acsnano.9b00686
ACS Nano 2019, 13, 7627−7643

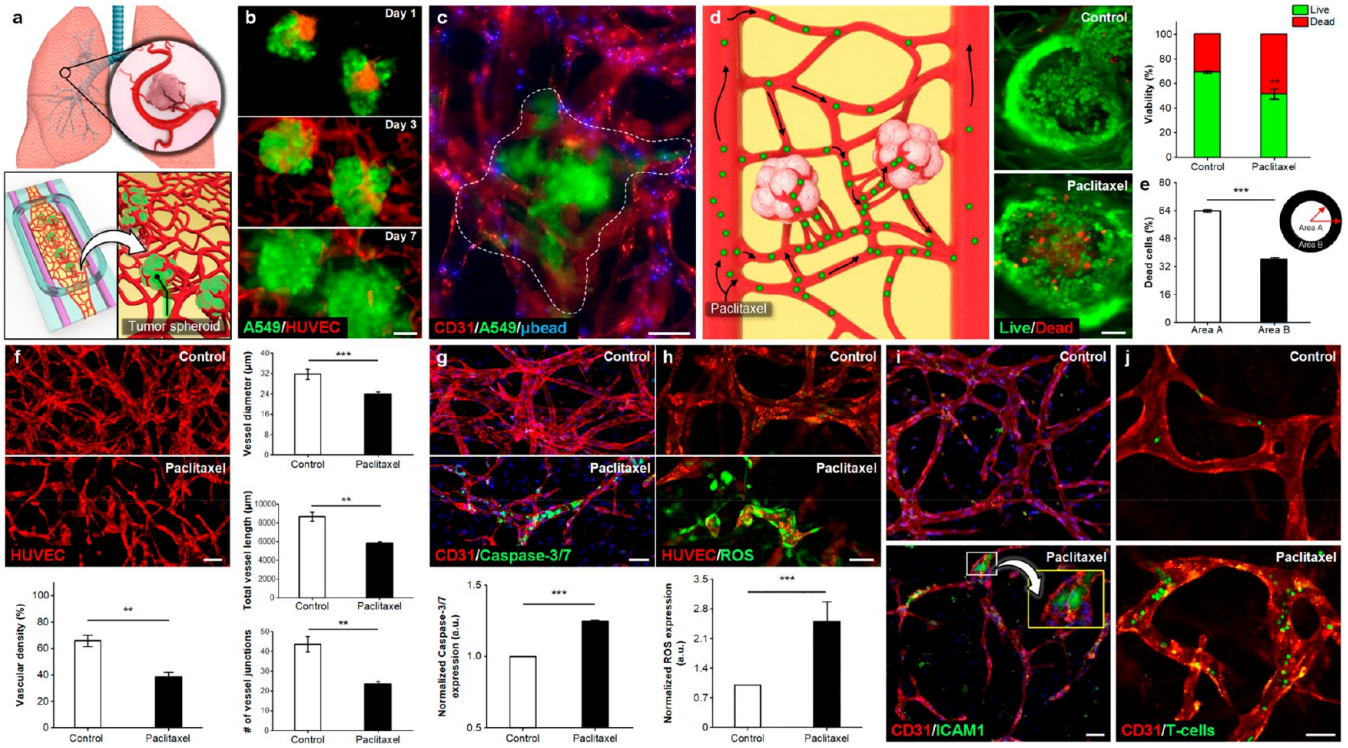

Figure 5. Vascularized solid tumor-on-a-chip for testing the efficacy and vascular toxicity of chemotherapy. a. To mimic malignant solid tumors in the lung, multicellular cancer spheroids are cocultured with endothelial cells and lung fibroblasts in the hydrogel compartment of our device to generate vascularized tumor constructs. b. During culture, the cancer spheroids composed of A549 cells (green) and RFP-HUVECs (red) grow in size and undergo structural integration with the surrounding vasculature formed by HUVECs embedded in the same hydrogel. Scale bar, 50 μm. c. A micrograph of a vascularized tumor spheroid perfused with fluorescent microbeads (blue). The outline of the spheroid is depicted with a white dotted line. Scale bar, 50 μm. d. For drug testing, the vascularized tumor construct is perfused with a clinical dose of paclitaxel. Drug treatment for 2 days leads to significant reduction in the viability of cancer cells, demonstrating the tumor killing effect of paclitaxel. Scale bar, 20 μm. e. In a given spheroid, the majority of dead cells are found in the inner two-thirds of the spheroid (area A). f. Our model also allows for detection and analysis of drug-induced vascular toxicities. Paclitaxel causes the loss and disintegration of the vasculature, resulting in significantly reduced vascular density, average vessel diameter, total vessel length, and junction number. Scale bar, 50 μm. Vascular perfusion with paclitaxel for 2 days also induces (g) endothelial apoptosis and (h) oxidative stress. Scale bars, 50 μm. i. The deleterious potential of paclitaxel to elicit vascular inflammation is shown by endothelial expression of ICAM-1. Scale bar, 50 μm. j. The activated endothelial lining of the paclitaxel-perfused vessels permits the recruitment of circulating immune cells as demonstrated by endothelial adhesion of T cells (green) injected into the engineered vasculature. Scale bar, 50 μm. Data are presented as mean ± SEM. $^{**}P < 0.01$ and $^{***}P < 0.001$ ($n = 3$).

known as Bruch's membrane that separates the neural retina from the capillary bed of the choroid (Figure 4a).[51,52] The oBRB plays an essential role in maintaining the homeostasis of the retina by regulating fluid and molecular transport between the outer retina and the blood in choroidal vessels.[53] Compromised integrity of the oBRB has been implicated in the development of retinal diseases such as age-related macular degeneration.[9,54,55]

To reconstitute this specialized barrier, we combined our vascular engineering platform with human inducible pluripotent stem cells (iPSCs) as a renewable source of RPEs. Specifically, we used human RPEs derived from long-term (140 days) culture and differentiation of iPSCs to form a confluent epithelial monolayer on the exposed surface of the underlying hydrogel construct (Figure 4b). The lower compartment of the device was used to mimic the microvascular bed of the choroid by culturing primary human retinal microvascular endothelial cells and choroidal fibroblasts in an ECM hydrogel made out of fibrin mixed with type I collagen, which has been shown to promote the structural and functional differentiation of RPEs.[56−58] As was the case with HUVECs and hAMECs, the retinal endothelial cells cultured in the hydrogel underwent vasculogenic self-assembly over a period of 7 days to develop a dense meshwork of perfusable microvessels that were roughly 10−25 μm in diameter (Figure 4c). In parallel, the iPSC-derived RPEs seeded into the opening of the culture chamber adhered to the surface of the hydrogel scaffold and proliferated continuously until they formed a densely packed monolayer of cuboidal cells. After 14 days of culture, the structural integrity of the epithelial barrier was demonstrated by a well-defined network of intercellular tight junctions (Figure 4d), which is a critical feature of the retinal pigment epithelium *in vivo* necessary for physiological barrier function of the oBRB.[59,60] Our characterization also revealed the production and deposition of basement membrane protein, laminin, on the basolateral side of the epithelial monolayer (Figure 4e). The laminin deposits accumulated underneath the epithelium and formed a thin sheet reminiscent of Bruch's membrane *in vivo*. Interestingly, this process of matrix synthesis and remodeling occurred in a vasculature-dependent manner. When the RPEs were cultured alone without the engineered vessels in the hydrogel compartment, the extent of laminin deposition was reduced by 50% as compared to that measured in the coculture system

DOI: 10.1021/acsnano.9b00686
ACS Nano 2019, 13, 7627−7643

at the same point (Figures 4f,g). This result illustrates significant vascular contributions to basement membrane formation in our model. Although the relevance of this finding to the *in vivo* context needs to be validated, our observation raises the possibility that the choroid may have the capacity to influence matrix production by RPEs and play an important role in the maintenance and remodeling of Bruch's membrane and the oBRB.

Another finding of interest was the development of dark granules in the cytoplasmic compartment of RPEs that were clearly visible in bright-field imaging of the epithelium (Figure 4h) and also showed strong immunofluorescence for melanosomes (Figure 4i). These results illustrate pigmentation of the cultured RPEs, which is an important characteristic of their *in vivo* counterparts that allows the oBRB to absorb scattered light for clear vision and to scavenge reactive radical species to protect the retina from oxidative damage.[53,61] Importantly, the expression of this key RPE phenotype was enhanced by the vasculature in the choroidal compartment, as evidenced by a more than 2.5-fold increase in immunohistochemical analysis of melanosome-containing RPEs in the oBRB model in comparison to a monoculture of RPEs (Figure 4j). When the RPEs in monoculture were treated with endothelial conditioned media, the level of melanosome expression did not show significant changes compared to the untreated monoculture group and remained substantially lower than that measured in the coculture model (Figure S6), suggesting the importance of the short-range interactions between the RPEs and the vasculature for RPE pigmentation. Many of the pigmented RPEs were also found to express high levels of RPE-specific markers such as RPE65 (Figure 4k). Similar to laminin deposition and pigmentation, the expression of RPE65 was significantly upregulated by coculture of RPEs with the underlying microvasculature (Figure 4l), highlighting the importance of vascular components for the induction of physiological phenotype in RPEs.

Taken together, these results demonstrate the suitability of the iPSC-derived RPE cells in coculture with retina-specific endothelial cells for the purpose of modeling the architecture and cellular phenotype of the oBRB in our microphysiological system. The compartmentalized design of our device made it possible to replicate the relative spatial arrangement of the retinal pigment epithelium and the underlying choroidal vascular bed in a more realistic manner than is possible with conventional models based on Transwell inserts.[62,63] As shown here, our system may provide a robust platform to create coculture models with capabilities to mimic the integrated organization of vascularized parenchymal tissues in various organs.

Microphysiological Model of Vascularized Solid Tumor for High-Content Drug Screening. The vasculature plays an important role in a wide variety of diseases. As exemplified by various types of cancer and inflammatory disorders, blood vessels are central to delivery and exchange of cells and soluble factors that mediate complex biological processes underlying the development of pathological conditions.[64] The vasculature can also contribute to disease progression and exacerbation by undergoing significant structural and functional changes to support growth, maintenance, and expansion of diseased tissues.[65,66] Despite extensive *in vivo* evidence, however, our ability to model and investigate the pathophysiological significance of the vasculature *in vitro* remains rudimentary. A key challenge in these types of studies has been the limited capacity of conventional *in* vitro techniques to model the vasculature in the integrated context of its associated tissues undergoing pathological processes. Motivated by this problem, we explored whether our microvascular engineering approach could be leveraged to mimic diseased human tissues that reside in vascularized 3D environments.

For this investigation, we used lung cancer as a model disease and developed a microphysiological system that combined the self-assembled perfusable microvasculature with 3D tumor spheroids (Figure 5a). As a first step to construct this model, we established a mixed coculture of human lung adenocarcinoma cells (A549) and endothelial cells (HUVECs) in low-attachment wells to form multicellular spheroids reminiscent of solid tumors in the lung. The composite cancer spheroids were then injected into our device and embedded in an ECM hydrogel scaffold that contained endothelial cells and lung fibroblasts. During culture, the spheroids became progressively larger, presumably due to the proliferation of cancer cells, while maintaining their spherical shape and structural integrity without significant cellular outgrowth (Figure 5b). Simultaneously, the endothelial cells in the hydrogel underwent proliferation and self-assembly into a 3D vascular network throughout the scaffold over a period of 7 days. During this process, most of the tumor spheroids were fully enveloped by the vasculature and appeared to be integrated with their surrounding microvessels (Figure 5b). Perfusability of the vascularized tumors and their local microenvironment was demonstrated by the flow of fluorescent microbeads through the vasculature in and around the cancer spheroids (Figure 5c).

Given the increasing attention to the potential of microphysiological systems for drug testing, we then investigated the feasibility of using our engineered tumor model as a screening platform to evaluate the effects of anticancer drugs. This study was conducted using paclitaxel as a model drug that represents cytotoxic chemotherapeutic agents in current clinical use for the treatment of solid tumors in various types of cancer including lung cancer.[67,68] To simulate intravascular drug delivery to solid tumors during chemotherapy, we injected clinical concentrations of paclitaxel into the endothelialized side channel and generated continuous flow through the engineered vasculature (Figure 5d). Vascular perfusion of our model under this condition for 2 days led to arrested growth and significant damage of the lung tumor constructs, resulting in approximately 20% reduction in the viability of cells in the cancer spheroids as compared to the vehicle control group (Figure 5d). It was noted that the drug-induced cytotoxicity showed spatial heterogeneity with the majority of dead cells found near the center of the spheroids (Figure 5e). This result is in contrast to the localized tumor-killing effect of paclitaxel at the outer surface of spheroids typically observed in traditional *in vitro* models based on static culture of avascular cancer spheroids (Figure S7). While further investigation is needed, this difference may be attributed to the vascularized architecture of our engineered tumor tissue that facilitated drug transport into the inner regions of the spheroids.

Another important goal of our study was to explore the use of the vascularized tumor model for the study of paclitaxel-induced vascular toxicities. This investigation was motivated by two lines of evidence suggesting the clinical significance and implications of endothelial toxicity due to chemotherapy. First, studies have discovered that classic cytotoxic drugs designed to

DOI: 10.1021/acsnano.9b00686
ACS Nano 2019, 13, 7627−7643

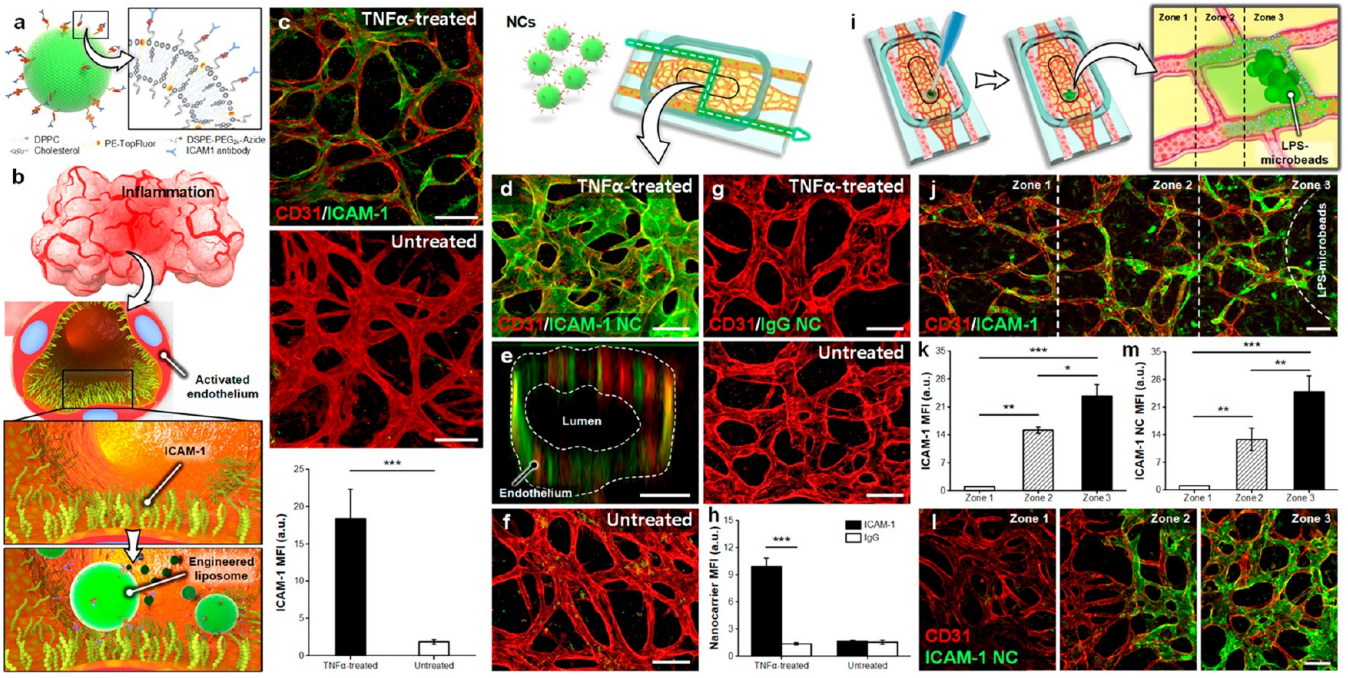

Figure 6. Vascular inflammation models for evaluation of nanoengineered drug carriers. a, b. A schematic diagram of azide-functionalized fluorescent DPPC-cholesterol liposomes. The monoclonal antibody against ICAM-1 coupled to their surface allows them to recognize and bind to ICAM-1 on the activated endothelial surface during inflammatory responses. c. Intravascular flow of TNF for 6 h results in endothelial expression of ICAM-1. Scale bar, 100 μm. d, e. The anti-ICAM-1 nanocarriers (NCs) adhere to the TNF-stimulated endothelial surface. Scale bars, (d) 100 μm and (e) 25 μm. f. The non-TNF-treated blood vessels show minimal liposome binding. Scale bar, 100 μm. g, h. The IgG-coupled liposomes do not bind to the blood vessels. Scale bar, 100 μm. i. Local inflammation is simulated by injecting LPS-soaked microbeads directly into the vascularized hydrogel through the opening of the culture chamber. j, k. The localized source of inflammation results in graded activation of endothelial ICAM-1. The expression level is inversely proportional to the distance from the LPS beads. Scale bar, 100 μm. l, m. Binding of anti-ICAM-1 NCs perfused through the vasculature corresponds to the spatial pattern of ICAM-1 activation, further demonstrating the active targeting capability of the liposomal NCs. Scale bar, 100 μm.

target cancer cells can also exert detrimental effects on the basic function of endothelial cells.[69] As a result, several cytotoxic cancer drugs, including paclitaxel, are now considered as potential therapeutic agents to disrupt the vasculature in the tumor microenvironment and to inhibit cancer angiogenesis.[70,71] Systematic and accurate preclinical evaluation of this added therapeutic value, however, has been challenged by the limited capacity of traditional *in vitro* cancer models to reproduce the vascularized architecture of solid tumors. Second, clinical evidence has shown that vascular toxicities due to anticancer drugs may be used as a predictive marker to identify asymptomatic patients at high risk of developing cardiovascular complications during the course of chemotherapy.[70] These studies highlight the potential clinical benefit of evaluating chemotherapy-induced endothelial dysfunction, but this line of investigation is still in need of advanced *in vitro* techniques to model and interrogate toxic responses of the tumor vasculature.

Therefore, we set out to test the utility of our engineered cancer model for analysis of adverse vascular responses to chemotherapy. To capture the complexity of such responses, our study relied on microfluorimetric techniques to measure the effect of paclitaxel on a range of phenotypic end points indicative of vascular structure and biochemical function. As shown in Figure 5f, the engineered vasculature perfused with a clinical dose of paclitaxel underwent marked structural changes illustrated by the disruption of its characteristic network architecture. Within 2 days of perfusion, vascular density decreased significantly due to a significant loss of endothelial lining in a large fraction of drug-treated vessels. Quantification of vascular architecture also revealed significant reduction in the average vessel diameter, total vessel length, and number of vessel junctions over the same period (Figure 5f). The detrimental effect of paclitaxel was further evidenced by the regression of the interconnected tubular network to disorganized endothelial chord-like structures, as well as significant reduction (Figure 5f). The drug-induced changes in vascular architecture were accompanied by the activation of apoptotic pathways in endothelial cells, as demonstrated by their robust expression of caspase-3/7 throughout the perfused vasculature (Figure 5g). These results are consistent with previous findings[72,73] and can be explained by the well-documented activity of paclitaxel to disrupt the microtubule network, which has been shown to cause detachment and apoptosis of endothelial cells.[70,71]

While endothelial cell death is central to chemotherapy-induced vascular toxicities, cytotoxic cancer drugs have the capacity to elicit various other types of endothelial dysfunction that contribute to adverse vascular responses.[74,75] For example, paclitaxel can promote the production of reactive oxygen species (ROS) in endothelial cells by increasing the activity of reduced nicotinamide adenine dinucleotide phosphate (NADPH), which can be injurious to the vasculature.[76,77] Consistent with these findings, paclitaxel treatment in our model led to a 2.5-fold increase in the level of ROS, as compared to the control group (Figure 5h). Given the established role of ROS as key mediators of inflammation,[78] we also examined whether paclitaxel triggered inflammatory

DOI: 10.1021/acsnano.9b00686
ACS Nano 2019, 13, 7627−7643

responses in the engineered vasculature. This study focused on endothelial expression of intercellular adhesion molecule 1 (ICAM-1) as a representative readout of vascular inflammation. In contrast to the vehicle control that yielded no measurable signals in immunohistochemical analysis of ICAM-1, positive staining was clearly visible in a significant fraction of vessels perfused with paclitaxel (Figure 5i). When human T lymphocytes were injected into the drug-treated vascular network, a large number of cells attached to the endothelial lining and remained adherent, further demonstrating drug-induced activation of endothelial cells (Figure 5j). Under the same flow conditions, however, the control devices showed negligible endothelial recruitment of lymphocytes.

Taken together, these data indicate that paclitaxel can induce endothelial oxidative stress and inflammation in our microengineered device, which have been suggested as the key potential mechanisms of cytotoxic drug-induced vascular toxicities.[76,77] It remains to be examined, however, how the toxic responses of the tumor-specific vasculature are different from those of normal blood vessels, which is an important consideration for the development of more effective anticancer drugs with reduced side effects.[79] Nevertheless, the results presented here show the possibility of using this model to develop a preclinical platform for high-content phenotypic analysis of vascular responses to chemotherapy.

Evaluation of Nanoengineered Drug Carriers in Vascular Inflammation Models. Advances in nanotechnology have led to the development of various colloidal particles of submicrometer size that can encapsulate and carry therapeutic payloads for nanomedicine applications.[80,81] Research has demonstrated that these nanocarriers provide a promising approach to increase the solubility and stability of drug compounds while also improving their pharmacokinetics and biodistribution.[82−85] Moreover, the physicochemical properties of nanocarriers can readily be engineered for controlled release and specific delivery of therapeutic agents, offering a means to minimize adverse off-target effects.[86−88] For the development of these specialized nanomaterials, traditional cell culture has proven instrumental in testing and optimizing the design of engineered drug delivery vehicles.[89,90] Conventional *in vitro* models, however, have limited capacity to accurately recapitulate transport and biological interactions of nanocarriers in the physiological 3D environment of vascularized and perfused human tissues. As a result, current methods of assessing the efficacy and safety of therapeutic nanoparticles rely predominantly on animal studies. Therefore, we asked if our microengineering platform could be used to construct advanced *in vitro* models for preclinical screening of nanoengineered drug carriers.

In this study, we selected liposomes as a model delivery system due to their well-established utility and potential for applications in nanomedicine.[91−93] Based on the central role of inflammation in the development and progression of a wide range of diseases,[94,95] the focus of our study was to examine the performance of liposomal drug carriers engineered to target the pathophysiological niche of inflamed tissues. For this investigation, we first generated azide-functionalized fluorescent DPPC-cholesterol liposomes with an average hydrodynamic diameter of 135 nm using thin film hydration techniques (Figure S8).[96] The surface of the liposomes was then functionalized with a monoclonal antibody against ICAM-1 (Figure 6a) to confer active targeting capabilities necessary for specific interaction with activated endothelial cells in the vasculature of inflamed tissues (Figure 6b).[93]

To test these engineered liposomes, we established a model of inflamed blood vessels by perfusing the self-assembled vasculature in our device with tumor necrosis factor (TNF)-α at 10 ng/mL for 6 h. The cytokine treatment did not induce significant changes in vascular architecture but was effective for eliciting inflammatory responses, as evidenced by a more than 6-fold increase in endothelial expression of ICAM-1 compared to the untreated group (Figure 6c). When the liposomes were injected into the TNF-treated vascular network, we observed abundant binding to the blood vessels during vascular perfusion (Figure 6d, Figure S9). Confocal microscopy revealed that the liposomes were bound to the endothelial lining of the vasculature and remained adherent after multiple steps of washing (Figure 6e). Under the same flow conditions, however, the control blood vessels without TNF stimulation exhibited nearly negligible vascular retention of the liposomes (Figure 6f,h; Figure S9). Importantly, when the ICAM-1 antibody was substituted with nonspecific immunoglobulin G (IgG), the vessels perfused with liposome-containing media showed no detectable fluorescence regardless of TNF treatment (Figure 6g). These results indicate that the functionalized liposomal nanocarriers have the ability to recognize and specifically bind to their target (ICAM-1) on the activated vascular endothelium.

While this study serves to verify the target-specificity of the engineered liposomes, our model based on global stimulation of the vasculature with TNF fails to mimic the reality of how the pathophysiological environment of inflamed tissues is created *in vivo*. In many cases, inflammation in the body is triggered in a localized manner, which gives rise to biochemical gradients of soluble pro-inflammatory mediators due to their diffusion from the local source of inflammation into the surrounding environment.[97,98] To capture this important aspect of the *in vivo* environment and model local inflammation, we generated lipopolysaccharide (LPS)-laden microbeads and injected them into the vascularized hydrogel through the open top of the culture chamber (Figure 6i). Our analysis of the vasculature after 4 h of incubation clearly showed spatially graded endothelial activation where the level of ICAM-1 expression was the highest in the vicinity of the LPS-microbeads and decreased gradually with increasing distance from the source of inflammation (Figure 6j,n). This is presumably because the engineered vessels were subjected to concentration gradients of LPS in the hydrogel scaffold and therefore became activated to varying degrees in a dose-dependent manner. Importantly, vascular perfusion of this model with anti-ICAM-1 liposomes resulted in corresponding zonation of their endothelial adhesion. As illustrated in Figure 6l, the vast majority of blood vessels in the region adjacent to the injected endotoxin beads exhibited strong fluorescence due to extensive binding of green fluorescent liposomes. The intensity of nanocarrier-generated fluorescence, however, was reduced significantly in other zones farther away from the microbeads (Figure 6m).

Taken together, these data provide *in vitro* evidence that supports the potential of our engineered nanocarriers for target-specific drug delivery. It should be noted that our study was focused on a limited set of end points and did not include parenchymal tissues that play an important role in inflammatory disease processes.[99] Despite these limitations, however, our results suggest the possibility of leveraging the advanced

DOI: 10.1021/acsnano.9b00686
ACS Nano 2019, 13, 7627−7643

capabilities to mimic vascularized and perfused 3D human tissues in microphysiological systems for preclinical evaluation of nanoengineered materials for therapeutic applications.

CONCLUSIONS

As exemplified by considerable recent advances in the development of organs-on-a-chip and microphysiological systems,[100] major efforts are being made toward developing *in vitro* technologies with advanced capabilities to emulate the integrated structure and function of human physiological systems. Our work represents an important contribution to this emerging trend in that it introduces a potentially powerful approach to reverse engineer the vasculature, which is an essential element of the human body. By simulating the natural process of *de novo* blood vessel formation during development, our method makes it possible to assemble 3D networks of interconnected and perfusable endothelial tubes that resemble microvascular beds *in vivo*. The microengineered cell culture system developed in this study also provides a modular platform to recapitulate the structural and functional association of blood vessels with other types of specialized cells and thus to create more realistic *in vitro* models of vascularized 3D tissues. For applications in drug development, our results suggest that these vascularized models are advantageous for simulating drug delivery in the native tissue microenvironment and may offer capabilities for high-content screening of drug-induced vascular dysfunction, as well as for the development of advanced therapeutic approaches.

While this study demonstrates the feasibility and potential of our microvascular engineering approach, it should be noted that it still leaves significant room for further investigations to improve the fidelity of the microengineered vasculature. Cellular heterogeneity is one of the important features of blood vessels and their perivascular environment that has yet to be fully recapitulated in our model. In particular, it is possible to incorporate pericytes that are intimately associated with the endothelial lining of the microvasculature and serve as a key regulator of vascular structure and function in a variety of physiological processes.[101,102] Similarly, immune cells found in the perivascular region, such as macrophages[103,104] and mast cells,[105] are another important resident cell population that may contribute to reconstituting physiological vascular responses to external stimuli in our model. Although our study has shown perfusability of the microengineered vessels, their functional characteristics need to be investigated and validated in a more rigorous manner. As demonstrated in the vascular toxicity study, for example, our data indicate transport of soluble intravascular content into the extravascular space, but more quantitative and systematic analysis of vascular permeability is required to improve our ability to engineer blood vessels that are more representative of their *in vivo* counterparts. Given the extensive evidence showing the importance of hemodynamics in the vascular system,[106,107] further research efforts may be necessary to engineer the characteristics of vascular perfusion (e.g., shear stress, pulsatility) with the goal of recapitulating the physiologically relevant hemodynamic microenvironment.

Our results have demonstrated that the open-top design makes it possible to increase the supply of nutrients and oxygen and to meet complex media requirements during coculture of multiple cell types necessary for generating complex 3D tissue models. On the other hand, this enabling design feature may also reflect the limitation of our approach as blood vessels in the body are fully capable of supporting the development and maintenance of various specialized tissues in a self-sufficient manner. Modeling this *in vivo*-like functional capacity in our engineered vasculature should be considered as an important goal for future investigations. Previous work on vascularized *in vitro* 3D tissue constructs may provide valuable insights and guidance for this effort.[14,108] Studies should also explore the possibility of leveraging our techniques to reconstruct different-sized blood vessels, which may then be combined to build a multiscale vascular model capable of mimicking the structural and functional hierarchy of the vascular system. As demonstrated in our study using cancer spheroids as a model system, our platform makes it possible to integrate 3D tissue constructs with perfusable vessels. Extending this approach to *in vitro* culture of organoids and tissue explants may provide a potential solution to address the major challenges associated with controlling and manipulating their local microenvironment in 3D culture systems.[109] Finally, efforts should be made to address the ultimate question of whether our advanced *in vitro* systems are more physiologically relevant and predictive of human responses than laboratory animals.

Our work represents a significant advance in our ability to reverse engineer the essential unit of the vascular system and its structural and functional integration with other types of specialized tissues. We believe that the 3D culture platform and biologically inspired tissue engineering strategy developed in this study will contribute to advancing the state-of-the-art for *in vitro* modeling of complex physiological systems for the study of human health and disease.

METHODS/EXPERIMENTAL DETAILS

Device Fabrication. We used standard soft lithography techniques to fabricate a medium reservoir and a poly-(dimethylsiloxane) (PDMS) slab patterned with recessed features of microchannels and a cell culture chamber as shown in Figure 1b. The cross-sectional dimensions of the cell culture chamber and the side microchannels were 1600 μm (width) × 400 μm (height) and 400 μm (width) × 400 μm (height), respectively (Figure S1). The size of the opening in the cell culture chamber was 1 mm (width) × 3 mm (length). The medium reservoir was produced by molding PDMS into a square ring with the dimensions of 12 mm (width) × 12 mm (length) × 4 mm (height). For fabrication of these components, PDMS (Sylgard 184, Dow Corning) base was mixed thoroughly with a curing agent at a weight ratio of 10:1 (base:curing agent) and poured onto 3D-printed masters (ProtoLab). After degassing, PDMS was fully cured in an oven maintained at 65 °C. The hardened PDMS was then removed from the molds, and inlet and outlet ports were made sideways in the channel slab to gain fluidic access to the microchannels and cell culture chamber. For device assembly, the PDMS slab containing channel features was stamped against a thin layer of uncured PDMS prepared by spin-coating at 1500 rpm for 5 min and sealed against a thin PDMS slab that was used as a bottom layer of the device. The same technique was used to bond the medium reservoir to the upper surface of the channel slab. The assembled device was baked at 65 °C to fully cure the PDMS adhesive layer.

Cell Culture. To demonstrate the proof-of-principle for engineering 3D microvascular beds in our device presented in Figures 1 and 2, we used primary human umbilical vein endothelial cells (HUVECs) and primary normal human lung fibroblasts (NHLFs). HUVECs and NHLFs were cultured in 25 cm^2 flasks according to the manufacturer's protocols using endothelial cell growth medium (EGM)-2 (CC-3162, Lonza) and fibroblast growth medium (FGM)-2 media (CC-3132, Lonza), respectively. Cells between passage 3 and 5 were used for device culture.

DOI: 10.1021/acsnano.9b00686
ACS Nano 2019, 13, 7627−7643

For modeling the adipose tissue (Figure 3), we used multipotent human adipose-derived stem cells (hASCs) (7510, ScienCell) and primary human adipose microvascular endothelial cells (hAMECs) (7200, ScienCell). The adipose and vascular cells were cultured and maintained with hASC (PM-1, Zenbio) and hAMEC (1001, ScienCell) growth media 25 cm^2 flasks following the protocols provided by the manufacturers. For best results, cells were used for microfluidic culture before they reach passage 6.

A microengineered model of the outer blood−retinal barrier (oBRB) shown in Figure 4was constructed using primary human retinal endothelial cells (ACBRI 181, Cell Systems), primary human ocular choroid fibroblasts (#6620, ScienCell), and induced pluripotent stem cell (iPSC)-derived human retinal pigment epithelial cells (RPEs). The endothelium growth medium (4Z0-500, Cell Systems) and fibroblast specific medium (#2301, ScienCell) were used to maintain the retinal endothelial cells and choroidal fibroblasts, respectively. For culture of iPSC-derived RPEs, the cells were cultured with specialized RPE-THT medium composed of 118 mL of DMEM/F12 (D6421, Sigma), 118 mL of alpha-MEM (M8042, Sigma), 2.5 mL of sodium pyruvate (11360-070, ThermoFisher), 2.5 mL of MEM-NEAA (11140-050, ThermoFisher), 1.25 mL of N1 supplement (N6530, Sigma), 1.25 mL of Glutamax (35050-061, ThermoFisher), 62.5 mg of Taurine (T0625, Sigma), 5 μg of hydrocortisone (H0396, Sigma), and 0.00325 μg of triiodothrionine (T5516, Sigma). Before use, cells were cultured in complete growth media in 75 cm^2 flasks according to the manufacture's protocol.

Formation of Cell-Laden ECM Hydrogel Scaffolds in the Microdevice. Prior to cell culture, the fully assembled device was first sterilized by exposing it to ultraviolet (UV) light (Electro-lite ELC-500) for at least 30 min. Subsequently, the cell culture chamber was filled with a buffer solution containing 0.2 mg/mL of sulfosuccinimidyl 6-(4′-azido-2′-nitrophenylamino)hexanoate (Sulfo-SANPAH, 13414, Covachem) and irradiated with 365 nm UV light for 10 min to create surface coating for enhanced adhesion of ECM hydrogel to PDMS surfaces of the cell culture chamber.

After rinsing with DPBS (356008, Corning) twice, removable templates were inserted into the device through the side microchannels (Figure 1d). We used a syringe needle with an outer diameter of 400 μm (Jensen Global) as a template. Once the needles were positioned in place, 20 μL of a cell suspension solution containing fibrinogen (10 mg/mL; F8630, Sigma), thrombin (1 U/mL; T7513, Sigma), aprotinin (0.15 U/mL; A1153, Sigma), HUVECs (2.5×10^6 cells/mL), and NHLFs (5×10^6 cells/mL) was gently injected into the cell culture chamber. The device was then left in a cell culture incubator at 37 °C and 5% CO_2 for 30 min. Upon completion of the gelation step, the needles were removed from the microchannels, and EGM-2 medium was added to the medium reservoir and the side microchannels.

Microfluidic Cell Culture. Following the formation of cell-laden fibrin hydrogel construct, the side microchannels were incubated with a fibronectin solution (25 μg/mL in PBS; 356008, Corning) for 3 h at 37 °C to create an ECM coating on the channel surface. Afterward, the channels were washed once with EGM-2, and 10 μL of HUVEC suspension (1×10^7 cells/mL) was introduced into both channels. The seeded cells were then allowed to attach to the channel surface over a period of 3 h. Once the cells established firm adhesion, external medium reservoirs were inserted into the channel inlets, and the outlet of each channel was connected to a syringe pump (Chemyx) operating on a withdrawal mode to generate continuous flow of culture media at a volumetric flow rate of 70 μL/h. This perfusion culture condition was maintained to allow the endothelial cells to form confluent monolayers on the surface of the hollow circular channels in the hydrogel scaffold created by the template needles and to induce anastomosis between the endothelium lining and the self-assembled vasculature in the hydrogel.

Testing of Vascular Perfusability. To investigate the perfusability of the engineered microvasculature, we used 75 kDa FITC-dextran (50 μg/mL in PBS; 46945, Sigma) and fluorescently labeled 1-μm microbeads (FluoSpheres; F-8815, ThermoFisher) as flow tracers. In the first step to generate flow through the vasculature, a fluid reservoir containing dye/bead solution was inserted into the inlet of one of the side microchannels while keeping its outlet blocked. Next, the inlet of the other side microchannel was sealed, but the outlet of this channel was left open. This configuration created a gradient of hydrostatic pressures across the hydrogel scaffold in a diagonal direction, providing driving force for the flow of fluorescent tracers through the vessels. Vascular perfusion was monitored and visualized using an epi-fluorescence microscope (Axio Observer D1, Zeiss).

Construction of the Adipose Tissue Model. To form vascularized adipose tissue in our microdevice, we first resuspended trypsinized hASCs and hAMECs in their growth media and mixed them with collagen type I (final concentration: 2 mg/mL; 354236, BD bioscience), fibrinogen (final concentration: 10 mg/mL, Sigma) and thrombin (final concentration: 1 U/mL, Sigma). The final concentrations of hASCs and hAMECs were 2.5×10^6 cells/mL and 5×10^6 cells/mL, respectively. The cell-containing hydrogel solution was then injected into the cell culture chamber of our microdevice, which was kept in a regular cell culture incubator for gelation. Once the template needles were removed, a 1:1 mixture of EGM-2 (22011, PromoCell) and subcutaneous basal medium (BM-1, ZenBio) was introduced into the top medium reservoir and the side microchannels. To induce adipogenesis, we used BM-1 supplemented with 20 nM of insulin (Actrapid, Novo Nodisk), 1 μM of dexamethason (D2915, Sigma), and 0.5 mM of 3-isobutyl-1-methylxanthine (IBMX, I7018, Sigma). This media condition was maintained for 7 days to induce the differentiation of hASCs into adipocytes. Without the adipogenic factors in the media, hASC differentiation did not occur during this period. After 7 days of culture, the supplements were replaced with 20 nM of insulin (Actrapid, Novo Nodisk) and 1 μM of dexamethason (D2915, Sigma). The cells were cultured with this maintenance medium for another 40 days. During this period, the media in the top reservoir and the microchannels were replenished every other day.

Detection and Quantification of Leptin. To analyze leptin secretion from the microengineered adipose tissue, the medium in the top reservoir was collected on days 7, 15, and 40 of culture. We used a human leptin ELISA kit (ab179884, abcam) to measure the concentration of leptin in the samples. In the first step of analysis, 50 μL of conditioned medium was added to each well, followed by the injection of another 50 μL of antibody solution. The plate was then sealed and incubated on an orbital shaker set at 400 rpm for 1 h at room temperature (RT). Subsequently, each well was washed 3 times with 350 μL of wash buffer provided by the manufacturer of the ELISA kit and received 100 μL of tetramethylbenzidine (TMB) solution. After 10 min of incubation in the dark, 100 μL of stop solution was added to each well. Finally, we used a multimode plate reader to measure the optical density of samples in each well (M200, Tecan).

Modeling of the Blood−Retinal Barrier. Retinal cells between passage 3 and 5 were used to create a model of the oBRB. First, we prepared 20 μL of a cell suspension solution containing type I collagen (final concentration: 2 mg/mL; 354236, BD bioscience), fibrinogen (final concentration: 10 mg/mL; F8630, Sigma), thrombin (final concentration: 1 U/mL; Sigma), aprotinin (final concentration: 0.15 U/mL; Sigma), primary human retinal microvascular endothelial cells (2.5×10^6 cells/mL), and primary human choroidal fibroblasts (5×10^6 cells/mL). This mixture solution was injected into the cell culture chamber and gelled in a cell culture incubator at 37 °C and 5% CO_2 for 30 min. Subsequently, the needles were removed from the microchannels, and EGM-2 medium was added to the top medium reservoir and the side microchannels. Following one-day incubation, retinal endothelial cells were seeded into the side channels and cultured under flow conditions to induce vascular anastomosis as described above. After 24 h, iPSC-derived human RPEs were plated and grown on the open top surface of the cell-laden ECM scaffold. Culture media were replaced every day.

Preparation of Lung Cancer Spheroids. Tumor spheroids were generated by using a A549 human lung adenocarcinoma cell line (Cell Biolabs, Inc.). A549 cells were cultured in ultralow attachment 96-well

DOI: 10.1021/acsnano.9b00686
ACS Nano 2019, 13, 7627−7643

plates (7007, Corning) with DMEM/F12 medium (D6421, Sigma) supplemented with 10% fetal bovine serum (FBS, 1082147, ThermoFisher) and 1% penicillin/streptomycin (P/S). For each well, 100 μL of cell suspension containing 1000 A549 cells were added, and the cells were allowed to settle and form a loose aggregate. After overnight culture, 100 μL of medium was pipetted into each well. A549 spheroids generated over a period of 3 days were harvested for use in our microdevices.

Production and Paclitaxel Treatment of the Vascularized Tumor Model. To create a vascularized lung tumor construct in our device, A549 spheroids were mixed with HUVECs and NHLFs in a hydrogel solution containing fibrinogen (final concentration: 10 mg/mL; F8630, Sigma), thrombin (final concentration: 1 U/mL; Sigma), and aprotinin (final concentration: 0.15 U/mL; Sigma). This solution was introduced into the device to form a fibrin construct in the culture chamber. The cells were cultured with EGM-2 for 7 days, during which the vascular network was formed and integrated with A549 spheroids embedded in the hydrogel. For paclitaxel treatment, the engineered vessels in the tumor construct were perfused with EGM-2 medium containing 2.5 μM paclitaxel for 48 h using the vascular perfusion technique described above.

Viability Assay of A549 Spheroids. Upon completion of paclitaxel treatment, a mixture of calcein AM and ethidium homodimer-1 (2 μM and 4 μM in culture medium, respectively) was introduced into the device and incubated at 37 °C for 20 min. Subsequently, the device was washed with DPBS three times and examined using an inverted epi-fluorescence microscope (Axio Observer D1, Zeiss). For quantitative analysis, we estimated the fraction of live and dead cells in each spheroid by measuring the average intensity of fluorescence generated by calcein AM and ethidium homodimer-1, respectively. In each device, five spheroids were used for our analysis.

Measurement of ROS Production and Caspase-3/7 Activation. Following paclitaxel treatment, the CellROXgreen (5 μM in DPBS; C10444, ThermoFisher) and CellEvent Caspase-3/7 Green (5 μM in DPBS; C10423, ThermoFisher) were used to measure oxidative stress and apoptosis of endothelial cells, respectively. The dye solutions were injected into the vasculature and incubated at 37 °C for 30 min. After three washing steps using DPBS, the vessels were imaged using an inverted epi-fluorescence microscope (Axio Observer D1, Zeiss). To generate quantitative data, we averaged fluorescence intensity measured from three regions of interest in each device.

T Lymphocytes Adhesion Assay. Human T lymphocytes were obtained from the Human Immunology Core at the University of Pennsylvania and cultured in RPMI-1640 (11875-093, ThermoFisher) with 10% FBS, 1% P/S, and 1 μg/mL of Phytohemagglutinin-M (PHA-M; 11082132001, Sigma) for 3 days. Subsequently, we changed the medium to RPMI-1640 with 10% FBS, 1% P/S, and 20 ng/mL of interleukin-2 (IL-2; 200-02, PeproTech) and cultured the cells for another three days. To test endothelial adhesion of T lymphocytes in our model, we labeled the cells with a fluorescent dye (CellTracker Green, ThermoFisher) and resuspended them in EGM-2 (Lonza) at the final concentration of 3×10^6 cells/mL. The cell suspension was then injected into the vessels through one of the side microchannels and allowed to flow through the vasculature for 1 h in a cell culture incubator. At the completion of perfusion, the device was washed with DPBS three times and examined to analyze the number of adhered T cells in the vascular network.

Liposome Preparation. Azide functionalized liposomes were prepared by thin film hydration techniques similar to those previously described.[96] Briefly, lipids DPPC (1,2-dipalmitoyl-*sn*-glycero-3-phosphocholine), cholesterol, Top Fluor PC (1-palmitoyl-2-(dipyrrometheneboron difluoride)undecanoyl-*sn*-glycero-3-phosphocholine), and azide PEG_{2000}DSPE (1,2-distearoyl-*sn*-glycero-3-phosphoethanolamine-*N*-[azido(polyethylene glycol)-2000]) (All phospholipids purchased from Avanti Polar Lipids, Alabaster, AL) in chloroform were combined in a borosilicate glass tube at a total lipid concentration of 20 mM. The lipid film was composed of 57.5 mol %:40 mol %:2 mol %:0.5 mol % DPPC/cholesterol/azide PEG_{2000}DSPE/Top Fluor PC. Lipid solutions were subjected to a constant stream of nitrogen gas until visibly dried and then lyophilized for 1 to 2 h to remove any residual solvent. Dried lipid films were hydrated with buffer (sterile Dulbecco's phosphate buffered saline (hereafter PBS), then went through three freeze–thaw cycles using liquid N_2/50 °C water bath, and then extruded 10 cycles through 200 nm polycarbonate filters (Avanti Polar Lipid). Dynamic light scattering (DLS) measurements of hydrodynamic particle size, distribution, and PDI were taken at each step of formulation from extrusion and subsequent modifications at 1:125 dilution in PBS using a Zetasizer Nano ZSP (Malvern Panalytical, Malvern UK). Liposome concentration following extrusion was assessed with Nanosight nanoparticle tracking analysis (Malvern).

Strained Alkyne Modification of Antibodies for Conjugation to Liposomes. IgG and anti-ICAM monoclonal-Antibody (mAb) were modified with dibenzylcyclooctyne-PEG_4-NHS ester (Jena Bioscience; Thuringia, Germany). The proteins, buffered in PBS and adjusted to pH 8.3 with 1 M $NaHCO_3$ buffer, were reacted for 1 h at RT at a ratio of 1:7 mAb:NHS ester PEG_4DBCO. Post-reaction, the mixture was buffer-exchanged with an amicon 10k MWCO centrifugal filter (MilliporeSigma, Burlington MA) to remove unreacted NHS ester PEG_4DBCO. The extent of modification was assessed *via* optical absorbance at 309 nm (corresponding to DBCO absorbance maximum, extinction coefficient 12000 M^{-1} cm^{-1}), compared to absorbance at 280 nm (corresponding to IgG absorbance, extinction coefficient 204000 M^{-1} cm^{-1}).

Ligand Conjugation to Liposomes. DBCO-modified antibodies (200 per liposome) were incubated with azide-functionalized liposomes overnight at RT. After incubation, the liposome–antibody mixture was characterized with dynamic light scattering (DLS), purified using size exclusion chromatography, concentrated to the original volume against centrifugal filters (Amicon), and again characterized with DLS.

Production of the Local Vascular Inflammation Model. LPS microbeads were produced by soaking gelatin microbeads (PCHMP-GB, Thies Technology) in 10 μg/mL LPS solution for 24 h. When vessel formation in the fibrin hydrogel (final concentration: 10 mg/mL; F8630, Sigma) was complete on day 7, the LPS microbeads were mixed with type I collagen (final concentration: 2 mg/mL, BD bioscience) and injected into a preformed small cavity within the fibrin scaffold. Upon gelation of the collagen–bead mixture (20 min at 37 °C), the device was incubated with EGM-2 for 4 h at 37 °C.

Liposome Binding Assay. Following the preparation of the local inflammation model, the anti-ICAM-1 liposomes were injected into the vessels through one of the side microchannels and allowed to flow through the vasculature. After 2 h of perfusion in a cell culture incubator, the device was washed with DPBS three times and inspected to measure liposome binding in the vascular network.

Immunostaining. For immunostaining, cells in our microfluidic devices were fixed in 4% paraformaldehyde for 15 min at RT, washed with DPBS, and permeabilized with 0.25% Triton X-100 for 10 min. Subsequently, a blocking step was performed using 3% bovine serum albumin (BSA) overnight at 4 °C. The cells were then incubated overnight at 4 °C with primary antibodies. For imaging of the self-assembled vessels, we used mouse monoclonal anti-CD31 (ab24590, 1:100, Abcam) and rabbit polyclonal antivimentin (ab92547, 1:200, Abcam) primary antibodies. For analysis of lipid droplets in the adipose tissue model, the cells were incubated with rabbit polyclonal antiperilipin-1 antibody (ab3526, 1:100, Abcam). Visualization of RPEs in the oBRB model was achieved by using rabbit polyclonal antizonula occludens-1 (anti-ZO-1, ab7878, 1:100, Abcam), mouse monoclonal anti-RPE 65 (ab13826, 1:1000, Abcam), rabbit monoclonal anti-Melanoma (ab137078, 1:400, Abcam), and mouse monoclonal F-actin (ab205, 1:100, Abcam) antibodies. Rabbit polyclonal antilaminin antibody (ab11575, 1:200, Abcam) was used to stain the basement membrane between RPEs and the choroid.

After incubation with primary antibody, the cells were washed twice with PBS and incubated for 1 h at RT with secondary antibody (A-11037, ThermoFisher; A-32723, ThermoFisher; ab150080 Abcam; ab150117, Abcam). We also used Hoechst (33342, ThermoFisher) for nuclear staining. Fluorescence images of the

DOI: 10.1021/acsnano.9b00686
ACS Nano 2019, 13, 7627–7643

cells were captured by an inverted epi-fluorescence microscope equipped with a confocal laser scanning module (LSM 800; Carl Zeiss, Germany). The obtained images were processed using the ZEN software (Zeiss, Germany).

SEM Imaging of Hydrogel Scaffolds. Scanning electron microscopy (SEM) was conducted at the CDB Microscopy Core (Perelman School of Medicine, University of Pennsylvania). The hydrogel scaffolds were washed three times with 50 mM Na-cacodylate buffer (pH 7.3) and fixed for 2 h with 2% glutaraldehyde in 50 mM Na-cacodylate buffer. Dehydration steps were then performed in 30%, 50%, 75%, 95%, and 100% ethanol for 1.5 h. Subsequently, the scaffolds were incubated for 20 min in 50% HMDS in ethanol followed by three changes of 100% HMDS (Sigma-Aldrich Co.) and overnight air-drying as described previously.[110] Finally, the samples were mounted on stubs and sputter coated with gold palladium. The specimens were observed and photographed using a Quanta 250 FEG scanning electron microscope (FEI, Hillsboro, OR, USA) at 10 kV accelerating voltage.

AFM Measurement for Hydrogel Stiffness. Atomic force microscopy (AFM, MFP-3D-BIO, Asylum) was used to characterize the mechanical property of hydrated hydrogel scaffolds used in the adipose and retina models shown in Figures 3 and 4. A Au coated cantilever (SCONT tip, NANOSENSORS) with a spring constant of 14.58 pN/nm and a pyramid indenter was used to obtain force–indentation curves. Young's modulus was calculated from the force indentation data using the AtomicJ software.

Statistical Analysis. Statistical significance of the obtained data was evaluated by a two-tailed *t* test. Data generated by three independent experiments were presented as mean ± SEM.

ASSOCIATED CONTENT

Supporting Information

The Supporting Information is available free of charge on the ACS Publications website at DOI: 10.1021/acsnano.9b00686.

Additional details on the dimensions of the device, the AFM measurement and SEM imaging of hydrogel scaffolds, the morphological features of blood vessels, the differentiation of hASCs, the engineered adipose tissue, the contribution of choroidal vasculature on RPE maturation, the drug-induced tumor toxicity, the characterization of nanocarriers, and the nanocarrier binding (PDF)

Movie showing continuous flow of 1 μm fluorescent particles observed through the vascular network (AVI)

AUTHOR INFORMATION

Corresponding Author

*(D.H.) E-mail: huhd@seas.upenn.edu.

ORCID

Jungwook Paek: 0000-0003-4624-1996

Sunghee E. Park: 0000-0002-2909-6507

Elizabeth D. Hood: 0000-0002-6829-8339

Author Contributions

○(J.P. and S.E.P.) These authors contributed equally to this work.

Notes

The authors declare no competing financial interest.

ACKNOWLEDGMENTS

We thank G. Al, M. Farrell, J. Seo, G.S. Worthen, and A. Georgescu for their input and technical assistance. This work was supported by the National Institutes of Health (NIH) (1DP2HL127720-01, 1UG3TR002198-01, 1UC4DK104196-01, U24DK076169), the Cancer Research Institute, the National Science Foundation (CMMI:15-48571), the Paul G. Allen Family Foundation, the Alternatives Research and Development Foundation, and the University of Pennsylvania. D.H. is a recipient of the NIH Director's New Innovator Award and the Cancer Research Institute Technology Impact Award.

REFERENCES

(1) Fishman, A. P. Endothelium: A Distributed Organ of Diverse Capabilities. *Ann. N. Y. Acad. Sci.* **1982**, *401*, 1–8.

(2) Durand, M. J.; Gutterman, D. D. Diversity in Mechanisms of Endothelium-Dependent Vasodilation in Health and Disease. *Microcirculation* **2013**, *20*, 239–247.

(3) Cines, D. B.; Pollak, E. S.; Buck, C. A.; Loscalzo, J.; Zimmerman, G. A.; McEver, R. P.; Pober, J. S.; Wick, T. M.; Konkle, B. A.; Schwartz, B. S.; Barnathan, E. S.; McCrae, K. R.; Hug, B. A.; Schmidt, A. M.; Stern, D. M. Endothelial Cells in Physiology and in the Pathophysiology of Vascular Disorders. *Blood* **1998**, *91*, 3527–3561.

(4) Pugsley, M. K.; Tabrizchi, R. The Vascular System. An Overview of Structure and Function. *J. Pharmacol. Toxicol. Methods* **2000**, *44*, 333–40.

(5) Rubin, L. L.; Staddon, J. M. The Cell Biology of the Blood-Brain Barrier. *Annu. Rev. Neurosci.* **1999**, *22*, 11–28.

(6) Clarkson, P.; Celermajer, D. S.; Donald, A. E.; Sampson, M.; Sorensen, K. E.; Adams, M.; Yue, D. K.; Betteridge, D. J.; Deanfield, J. E. Impaired Vascular Reactivity in Insulin-Dependent Diabetes Mellitus Is Related to Disease Duration and Low Density Lipoprotein Cholesterol Levels. *J. Am. Coll. Cardiol.* **1996**, *28*, 573–579.

(7) Ziccardi, P.; Nappo, F.; Giugliano, G.; Esposito, K.; Marfella, R.; Cioffi, M.; D'Andrea, F.; Molinari, A. M.; Giugliano, D. Reduction of Inflammatory Cytokine Concentrations and Improvement of Endothelial Functions in Obese Women after Weight Loss over One Year. *Circulation* **2002**, *105*, 804–809.

(8) Panza, J. A.; Quyyumi, A. A.; Callahan, T. S.; Epstein, S. E. Effect of Antihypertensive Treatment on Endothelium-Dependent Vascular Relaxation in Patients with Essential Hypertension. *J. Am. Coll. Cardiol.* **1993**, *21*, 1145–1151.

(9) Ferrara, N. Vascular Endothelial Growth Factor and Age-Related Macular Degeneration: from Basic Science to Therapy. *Nat. Med.* **2010**, *16*, 1107–1111.

(10) Pezzella, F. Cancer and Blood Vessels: A Complex Relationship. *J. Can. Sci. Res.* **2016**, DOI: 10.4172/2576-1447.1000S1-002.

(11) Chrobak, K. M.; Potter, D. R.; Tien, J. Formation of Perfused, Functional Microvascular Tubes. *Microvasc. Res.* **2006**, *71*, 185–196.

(12) Booth, R.; Noh, S.; Kim, H. A Multiple-Channel, Multiple-Assay Platform for Characterization of Full-Range Shear Stress Effects on Vascular Endothelial Cells. *Lab Chip* **2014**, *14*, 1880–1890.

(13) Zahedmanesh, H.; Lally, C. Multiscale Modeling in Vascular Disease and Tissue Engineering. In *Multiscale Computer Modeling in Biomechanics and Biomedical Engineering*; Gefen, A., Ed.; Springer Berlin Heidelberg: Berlin, Heidelberg, 2013; pp 241–258.

(14) Miller, J. S.; Stevens, K. R.; Yang, M. T.; Baker, B. M.; Nguyen, D. H.; Cohen, D. M.; Toro, E.; Chen, A. A.; Galie, P. A.; Yu, X.; Chaturvedi, R.; Bhatia, S. N.; Chen, C. S. Rapid Casting of Patterned Vascular Networks for Perfusable Engineered Three-Dimensional Tissues. *Nat. Mater.* **2012**, *11*, 768–774.

(15) Scharrer, E. The Functional Significance of the Capillary Bed in the Brain of the Opossum. *Anat. Rec.* **1939**, *75*, 319–340.

(16) Maton, A. *Human Biology and Health*; Prentice Hall: Englewood Cliffs, NJ, 1993.

(17) Hasan, A.; Paul, A.; Vrana, N. E.; Zhao, X.; Memic, A.; Hwang, Y. S.; Dokmeci, M. R.; Khademhosseini, A. Microfluidic Techniques for Development of 3D Vascularized Tissue. *Biomaterials* **2014**, *35*, 7308–7325.

(18) Ehsan, S. M.; Welch-Reardon, K. M.; Waterman, M. L.; Hughes, C. C.; George, S. C. A Three-Dimensional *In Vitro* Model of Tumor Cell Intravasation. *Integr. Biol.* **2014**, *6*, 603–610.

DOI: 10.1021/acsnano.9b00686
ACS Nano 2019, 13, 7627–7643

(19) Wang, X.; Phan, D. T.; Sobrino, A.; George, S. C.; Hughes, C. C.; Lee, A. P. Engineering Anastomosis Between Living Capillary Networks and Endothelial Cell-Lined Microfluidic Channels. *Lab Chip* **2016**, *16*, 282−290.
(20) Kim, S.; Lee, H.; Chung, M.; Jeon, N. L. Engineering of Functional, Perfusable 3D Microvascular Networks on a Chip. *Lab Chip* **2013**, *13*, 1489−1500.
(21) Nashimoto, Y.; Hayashi, T.; Kunita, I.; Nakamasu, A.; Torisawa, Y. S.; Nakayama, M.; Takigawa-Imamura, H.; Kotera, H.; Nishiyama, K.; Miura, T.; Yokokawa, R. Integrating Perfusable Vascular Networks with a Three-Dimensional Tissue in a Microfluidic Device. *Integr. Biol.* **2017**, *9*, 506−518.
(22) Oh, S.; Ryu, H.; Tahk, D.; Ko, J.; Chung, Y.; Lee, H. K.; Lee, T. R.; Jeon, N. L. Open-Top" Microfluidic Device for *In Vitro* Three-Dimensional Capillary Beds. *Lab Chip* **2017**, *17*, 3405−3414.
(23) Yeon, J. H.; Ryu, H. R.; Chung, M.; Hu, Q. P.; Jeon, N. L. *In Vitro* Formation and Characterization of a Perfusable Three-Dimensional Tubular Capillary Network in Microfluidic Devices. *Lab Chip* **2012**, *12*, 2815−2822.
(24) Chen, M. B.; Whisler, J. A.; Fröse, J.; Yu, C.; Shin, Y.; Kamm, R. D. On-Chip Human Microvasculature Assay for Visualization and Quantitation of Tumor Cell Extravasation Dynamics. *Nat. Protoc.* **2017**, *12*, 865−880.
(25) Whisler, J. A.; Chen, M. B.; Kamm, R. D. Control of Perfusable Microvascular Network Morphology Using a Multiculture Microfluidic System. *Tissue Eng., Part C* **2014**, *20*, 543−552.
(26) Chen, Y. C.; Lin, R. Z.; Qi, H.; Yang, Y.; Bae, H.; Melero-Martin, J. M.; Khademhosseini, A. Functional Human Vascular Network Generated in Photocrosslinkable Gelatin Methacrylate Hydrogels. *Adv. Funct. Mater.* **2012**, *22*, 2027−2039.
(27) Bajaj, P.; Schweller, R. M.; Khademhosseini, A.; West, J. L.; Bashir, R. 3D Biofabrication Strategies for Tissue Engineering and Regenerative Medicine. *Annu. Rev. Biomed. Eng.* **2014**, *16*, 247−276.
(28) Linville, R. M.; Boland, N. F.; Covarrubias, G.; Price, G. M.; Tien, J. Physical and Chemical Signals That Promote Vascularization of Capillary-Scale Channels. *Cell. Mol. Bioeng.* **2016**, *9*, 73−84.
(29) Zhang, W.; Wray, L. S.; Rnjak-Kovacina, J.; Xu, L.; Zou, D.; Wang, S.; Zhang, M.; Dong, J.; Li, G.; Kaplan, D. L.; Jiang, X. Vascularization of Hollow Channel-Modified Porous Silk Scaffolds with Endothelial Cells for Tissue Regeneration. *Biomaterials* **2015**, *56*, 68−77.
(30) Yancopoulos, G. D.; Davis, S.; Gale, N. W.; Rudge, J. S.; Wiegand, S. J.; Holash, J. Vascular-Specific Growth Factors and Blood Vessel Formation. *Nature* **2000**, *407*, 242−248.
(31) Morin, K. T.; Tranquillo, R. T. *In Vitro* Models of Angiogenesis and Vasculogenesis in Fibrin Gel. *Exp. Cell Res.* **2013**, *319*, 2409−2417.
(32) Diaz-Santana, A.; Shan, M.; Stroock, A. D. Endothelial Cell Dynamics during Anastomosis *In Vitro*. *Integr. Biol.* **2015**, *7*, 454−466.
(33) Song, J. W.; Bazou, D.; Munn, L. L. Anastomosis of Endothelial Sprouts Forms New Vessels in aTissue Analogue of Angiogenesis. *Integr. Biol.* **2012**, *4*, 857−862.
(34) Rosen, E. D.; Spiegelman, B. M. Adipocytes as Regulators of Energy Balance and Glucose Homeostasis. *Nature.* **2006**, *444*, 847−853.
(35) Tilg, H.; Moschen, A. R. Adipocytokines: Mediators Linking Adipose Tissue, Inflammation and Immunity. *Nat. Rev. Immunol.* **2006**, *6*, 772−783.
(36) Gray, S. L.; Vidal-Puig, A. J. Adipose Tissue Expandability in the Maintenance of Metabolic Homeostasis. *Nutr. Rev.* **2007**, *65*, S7−S12.
(37) Chen, C. W.; Corselli, M.; Peault, B.; Huard, J. Human Blood-Vessel-Derived Stem Cells for Tissue Repair and Regeneration. *J. Biomed. Biotechnol.* **2012**, *2012*, 597439.
(38) Butler, J. M.; Kobayashi, H.; Rafii, S. Instructive Role of the Vascular Niche in Promoting Tumour Growth and Tissue Repair by Angiocrine Factors. *Nat. Rev. Cancer* **2010**, *10*, 138−146.
(39) Bouwman, F.; Renes, J.; Mariman, E. A Combination of Protein Profiling and Isotopomer Analysis Using Matrix-Assisted Laser Desorption/Ionization-Time of Flight Mass Spectrometry Reveals an Active Metabolism of the Extracellular Matrix of 3T3-L1 Adipocytes. *Proteomics* **2004**, *4*, 3855−3863.
(40) Mariman, E. C.; Wang, P. Adipocyte Extracellular Matrix Composition, Dynamics and Role in Obesity. *Cell. Mol. Life Sci.* **2010**, *67*, 1277−1292.
(41) Chun, T. H.; Hotary, K. B.; Sabeh, F.; Saltiel, A. R.; Allen, E. D.; Weiss, S. J. A Pericellular Collagenase Directs the 3-Dimensional Development of White Adipose Tissue. *Cell* **2006**, *125*, 577−591.
(42) Guilak, F.; Cohen, D. M.; Estes, B. T.; Gimble, J. M.; Liedtke, W.; Chen, C. S. Control of Stem Cell Fate by Physical Interactions with the Extracellular Matrix. *Cell Stem Cell.* **2009**, *5*, 17−26.
(43) Smith, L. R.; Cho, S.; Discher, D. E. Stem Cell Differentiation Is Regulated by Extracellular Matrix Mechanics. *Physiology* **2018**, *33*, 16−25.
(44) Huebsch, N.; Arany, P. R.; Mao, A. S.; Shvartsman, D.; Ali, O. A.; Bencherif, S. A.; Rivera-Feliciano, J.; Mooney, D. J. Harnessing Traction-Mediated Manipulation of the Cell/Matrix Interface to Control Stem-Cell Fate. *Nat. Mater.* **2010**, *9*, 518−526.
(45) Freiman, A.; Shandalov, Y.; Rozenfeld, D.; Shor, E.; Segal, S.; Ben-David, D.; Meretzki, S.; Egozi, D.; Levenberg, S. Adipose-Derived Endothelial and Mesenchymal Stem Cells Enhance Vascular Network Formation on Three-Dimensional Constructs In Vitro. *Stem Cell Res. Ther.* **2016**, *7*, 5.
(46) Sztalryd, C.; Brasaemle, D. L. The Perilipin Family of Lipid Droplet Proteins: Gatekeepers of Intracellular Lipolysis. *Biochim. Biophys. Acta, Mol. Cell Biol. Lipids.* **2017**, *1862*, 1221−1232.
(47) Itabe, H.; Yamaguchi, T.; Nimura, S.; Sasabe, N. Perilipins: A Diversity of Intracellular Lipid Droplet Proteins. *Lipids Health Dis.* **2017**, *16*, 83.
(48) Cao, Y. Adipose Tissue Angiogenesis as a Therapeutic Target for Obesity and Metabolic Diseases. *Nat. Rev. Drug Discovery* **2010**, *9*, 107−115.
(49) Harris, R. B. Direct and Indirect Effects of Leptin on Adipocyte Metabolism. *Biochim. Biophys. Acta, Mol. Basis Dis.* **2014**, *1842*, 414−423.
(50) Stern, J. H.; Rutkowski, J. M.; Scherer, P. E. Adiponectin, Leptin, and Fatty Acids in the Maintenance of Metabolic Homeostasis through Adipose Tissue Crosstalk. *Cell Metab.* **2016**, *23*, 770−784.
(51) Cunha-Vaz, J.; Bernardes, R.; Lobo, C. Blood-Retinal Barrier. *Eur. J. Ophthalmol.* **2011**, *21*, 3−9.
(52) Campbell, M.; Humphries, P. The Blood-Retina Barrier: Tight Junctions and Barrier Modulation. *Adv. Exp. Med. Biol.* **2013**, *763*, 70−84.
(53) Bhutto, I.; Lutty, G. Understanding Age-Related Macular Degeneration (AMD): Relationships between the Photoreceptor/Retinal Pigment Epithelium/Bruch's Membrane/Choriocapillaris Complex. *Mol. Aspects Med.* **2012**, *33*, 295−317.
(54) Jager, R. D.; Mieler, W. F.; Miller, J. W. Age-Related Macular Degeneration. *N. Engl. J. Med.* **2008**, *358*, 2606−2617.
(55) Ambati, J.; Fowler, B. J. Mechanisms of Age-Related Macular Degeneration. *Neuron* **2012**, *75*, 26−39.
(56) Kamao, H.; Mandai, M.; Okamoto, S.; Sakai, N.; Suga, A.; Sugita, S.; Kiryu, J.; Takahashi, M. Characterization of Human Induced Pluripotent Stem Cell-Derived Retinal Pigment Epithelium Cell Sheets Aiming for Clinical Application. *Stem Cell Rep.* **2014**, *2*, 205−218.
(57) Nugroho, R. W. N.; Harjumäki, R.; Zhang, X.; Lou, Y. R.; Yliperttula, M.; Valle-Delgado, J. J.; Österberg, M. Quantifying the Interactions between Biomimetic Biomaterials - Collagen I, Collagen IV, Laminin 521 and Cellulose Nanofibrils - by Colloidal Probe Microscopy. *Colloids Surf., B* **2019**, *173*, 571−580.
(58) Sorkio, A. E.; Vuorimaa-Laukkanen, E. P.; Hakola, H. M.; Liang, H.; Ujula, T. A.; Valle-Delgado, J. J.; Österberg, M.; Yliperttula, M. L.; Skottman, H. Biomimetic Collagen I and IV Double Layer Langmuir-Schaefer Films as Microenvironment for Human Pluripotent Stem Cell Derived Retinal Pigment Epithelial Cells. *Biomaterials* **2015**, *51*, 257−269.

DOI: 10.1021/acsnano.9b00686
ACS Nano 2019, 13, 7627−7643

(59) Rizzolo, L. J. Development and Role of Tight Junctions in the Retinal Pigment Epithelium. *Int. Rev. Cytol.* **2007**, *258*, 195−234.
(60) Rizzolo, L. J.; Peng, S.; Luo, Y.; Xiao, W. Integration of Tight Junctions and Claudins with the Barrier Functions of the Retinal Pigment Epithelium. *Prog. Retinal Eye Res.* **2011**, *30*, 296−323.
(61) Boulton, M. E. Studying Melanin and Lipofuscin in RPE Cell Culture Models. *Exp. Eye Res.* **2014**, *126*, 61−67.
(62) Geisen, P.; McColm, J. R.; Hartnett, M. E. Choroidal Endothelial Cells Transmigrate across the Retinal Pigment Epithelium but Do Not Proliferate in Response to Soluble Vascular Endothelial Growth Factor. *Exp. Eye Res.* **2006**, *82*, 608−619.
(63) Song, H. B.; Jun, H. O.; Kim, J. H.; Lee, Y. H.; Choi, M. H.; Kim, J. H. Disruption of Outer Blood-Retinal Barrier by Toxoplasma Gondii-Infected Monocytes Is Mediated by Paracrinely Activated FAK Signaling. *PLoS One* **2017**, *12*, No. e0175159.
(64) Khazaei, M.; Moien-Afshari, F.; Laher, I. Vascular Endothelial Function in Health and Diseases. *Pathophysiology* **2008**, *15*, 49−67.
(65) Goel, S.; Duda, D. G.; Xu, L.; Munn, L. L.; Boucher, Y.; Fukumura, D.; Jain, R. K. Normalization of the Vasculature for Treatment of Cancer and Other Diseases. *Physiol. Rev.* **2011**, *91*, 1071−1121.
(66) Roudsari, L. C.; West, J. L. Studying the Influence of Angiogenesis in *In Vitro* Cancer Model Systems. *Adv. Drug Delivery Rev.* **2016**, *97*, 250−259.
(67) Rowinsky, E. K. Clinical Pharmacology of Taxol. *J. Natl. Cancer Inst. Monogr.* **1993**, *15*, 25−37.
(68) Ramalingam, S.; Belani, C. P. Paclitaxel for Non-Small Cell Lung Cancer. *Expert Opin. Pharmacother.* **2004**, *5*, 1771−1780.
(69) Svilaas, T.; Lefrandt, J. D.; Gietema, J. A.; Kamphuisen, P. W. Long-Term Arterial Complications of Chemotherapy in Patients with Cancer. *Thromb. Res.* **2016**, *140*, S109−S118.
(70) Soultati, A.; Mountzios, G.; Avgerinou, C.; Papaxoinis, G.; Pectasides, D.; Dimopoulos, M.; Papadimitriou, C. Endothelial Vascular Toxicity from Chemotherapeutic Agents: Preclinical Evidence and Clinical Implications. *Cancer Treat. Rev.* **2012**, *38*, 473−484.
(71) Cameron, A. C.; Touyz, R. M.; Lang, N. N. Vascular Complications of Cancer Chemotherapy. *Can. J. Cardiol.* **2016**, *32*, 852−862.
(72) Semb, K. A.; Aamdal, S.; Oian, P. Capillary Protein Leak Syndrome Appears to Explain Fluid Retention in Cancer Patients Who Receive Docetaxel Treatment. *J. Clin. Oncol.* **1998**, *16*, 3426−3432.
(73) Vassilakopoulou, M.; Mountzios, G.; Papamechael, C.; Protogerou, A.D.; Aznaouridis, K.; Katsichti, P.; Venetsanou, K.; Dimopoulos, M.-A.; Ikonomidis, I.; Papadimitriou, C.A. Paclitaxel Chemotherapy and Vascular Toxicity as Assessed by Flow-Mediated and Nitrate-Mediated Vasodilatation. *Vasc. Pharmacol.* **2010**, *53*, 115−121.
(74) Clements, M. K.; Jones, C. B.; Cumming, M.; Daoud, S. S. Antiangiogenic Potential of Camptothecin and Topotecan. *Cancer Chemother. Pharmacol.* **1999**, *44*, 411−416.
(75) Vacca, A.; Ribatti, D.; Iurlaro, M.; Merchionne, F.; Nico, B.; Ria, R.; Dammacco, F. Docetaxel *Versus* Paclitaxel for Antiangiogenesis. *J. Hematother. Stem Cell Res.* **2002**, *11*, 103−118.
(76) Serizawa, K.; Yogo, K.; Aizawa, K.; Tashiro, Y.; Takahari, Y.; Sekine, K.; Suzuki, T.; Ishizuka, N.; Ishida, H. Paclitaxel-Induced Endothelial Dysfunction in Living Rats Is Prevented by Nicorandil *via* Reduction of Oxidative Stress. *J. Pharmacol. Sci.* **2012**, *119*, 349−358.
(77) Alexandre, J.; Hu, Y.; Lu, W.; Pelicano, H.; Huang, P. Novel Action of Paclitaxel Against Cancer Cells: Bystander Effect Mediated by Reactive Oxygen Species. *Cancer Res.* **2007**, *67*, 3512−3517.
(78) Mittal, M.; Siddiqui, M. R.; Tran, K.; Reddy, S. P.; Malik, A. B. Reactive Oxygen Species in Inflammation and Tissue Injury. *Antioxid. Redox Signaling* **2014**, *20*, 1126−1167.
(79) Michailidou, M.; Brown, H. K.; Lefley, D. V.; Evans, A.; Cross, S. S.; Coleman, R. E.; Brown, N. J.; Holen, I. Microvascular Endothelial Cell Responses *In Vitro* and *In Vivo*: Modulation by Zoledronic Acid and Paclitaxel? *J. Vasc. Res.* **2010**, *47*, 481−493.
(80) De Jong, W. H.; Borm, P. J. Drug Delivery and Nanoparticles: Applications and Hazards. *Int. J. Nanomed.* **2008**, *3*, 133−149.
(81) Duncan, R. The Dawning Era of Polymer Therapeutics. *Nat. Rev. Drug Discovery* **2003**, *2*, 347−360.
(82) Senior, J.; Gregoriadis, G. Is Half-Life of Circulating Liposomes Determined by Changes in Their Permeability? *FEBS Lett.* **1982**, *145*, 109−114.
(83) Seki, J.; Sonoke, S.; Saheki, A.; Fukui, H.; Sasaki, H.; Mayumi, T. A Nanometer Lipid Emulsion, Lipid Nano-Sphere (LNS), as a Parenteral Drug Carrier for Passive Drug Targeting. *Int. J. Pharm.* **2004**, *273*, 75−83.
(84) Wissing, S. A.; Kayser, O.; Müller, R. H. Solid Lipid Nanoparticles for Parental Drug Delivery. *Adv. Drug Delivery Rev.* **2004**, *56*, 1257−1272.
(85) Panyam, J.; Zhou, W. Z.; Prabha, S.; Sahoo, S. K.; Labhasetwar, V. Rapid Endo-Lysosomal Escape of Poly(DL-Lactide-Co-Glycolide) Nanoparticles: Implications for Drug and Gene Delivery. *FASEB J.* **2002**, *16*, 1217−1226.
(86) Muzykantov, V.; Muro, S. Targeting Delivery of Drugs in the Vascular System. *Int. J. Transp. Phenom.* **2011**, *12*, 41−49.
(87) Koren, E.; Torchilin, V. P. Drug Carriers for Vascular Drug Delivery. *IUBMB Life* **2011**, *63*, 586−595.
(88) Ferrari, M. Cancer Nanotechnology: Opportunities and Challenges. *Nat. Rev. Cancer* **2005**, *5*, 161−171.
(89) Farokhzad, O. C.; Khademhosseini, A.; Jon, S.; Hermmann, A.; Cheng, J.; Chin, C.; Kiselyuk, A.; Teply, B.; Eng, G.; Langer, R. Microfluidic System for Studying the Interaction of Nanoparticles and Microparticles with Cells. *Anal. Chem.* **2005**, *77*, 5453−5459.
(90) Ahn, J.; Ko, J.; Lee, S.; Yu, J.; Kim, Y.; Jeon, N. L. Microfluidics in Nanoparticle Drug Delivery; from Synthesis to Pre-Clinical Screening. *Adv. Drug Delivery Rev.* **2018**, *128*, 29−53.
(91) Mainardes, R. M.; Silva, L. P. Drug Delivery Systems: Past, Present, and Future. *Curr. Drug Targets* **2004**, *5*, 449−455.
(92) Moghimi, S. M.; Szebeni, J. Stealth Liposomes and Long Circulating Nanoparticles: Critical Issues in Pharmacokinetics, Opsonization and Protein-Binding Properties. *Prog. Lipid Res.* **2003**, *42*, 463−478.
(93) Hood, E. D.; Greineder, C. F.; Shuvaeva, T.; Walsh, L.; Villa, C. H.; Muzykantov, V. R. Vascular Targeting of Radiolabeled Liposomes with Bio-Orthogonally Conjugated Ligands: Single Chain Fragments Provide Higher Specificity than Antibodies. *Bioconjugate Chem.* **2018**, *29*, 3626−3637.
(94) Medzhitov, R. Inflammation 2010: New Adventures of an Old Flame. *Cell* **2010**, *140*, 771−776.
(95) Rajendran, P.; Rengarajan, T.; Thangavel, J.; Nishigaki, Y.; Sakthisekaran, D.; Sethi, G.; Nishigaki, I. The Vascular Endothelium and Human Diseases. *Int. J. Biol. Sci.* **2013**, *9*, 1057−1069.
(96) Hood, E. D.; Greineder, C. F.; Dodia, C.; Han, J.; Mesaros, C.; Shuvaev, V. V.; Blair, I. A.; Fisher, A. B.; Muzykantov, V. R. Antioxidant Protection by PECAM-Targeted Delivery of a Novel NADPH-Oxidase Inhibitor to the Endothelium *In Vitro* and *In Vivo*. *J. Controlled Release* **2012**, *163*, 161−169.
(97) Vodovotz, Y.; Csete, M.; Bartels, J.; Chang, S.; An, G. Translational Systems Biology of Inflammation. *PLoS Comput. Biol.* **2008**, *4*, No. e1000014.
(98) Vodovotz, Y. Deciphering the Complexity of Acute Inflammation Using Mathematical Models. *Immunol. Res.* **2006**, *36*, 237−245.
(99) Kemp, W.; Burns, D. K.; Brown, T. G. Inflammation and Repair. In *Pathology: The Big Picture*; McGraw-Hill Education: 2007; Chapter 2, pp 13−22.
(100) Esch, E. W.; Bahinski, A.; Huh, D. Organs-On-Chips at the Frontiers of Drug Discovery. *Nat. Rev. Drug Discovery* **2015**, *14*, 248−260.
(101) Bergers, G.; Song, S. The Role of Pericytes in Blood-Vessel Formation and Maintenance. *Neuro-Oncology.* **2005**, *7*, 452−464.
(102) Koike, N.; Fukumura, D.; Gralla, O.; Au, P.; Schechner, J. S.; Jain, R. K. Tissue Engineering: Creation of Long-Lasting Blood Vessels. *Nature* **2004**, *428*, 138−139.

DOI: 10.1021/acsnano.9b00686
ACS Nano 2019, 13, 7627−7643

(103) Moore, E. M.; West, J. L. Harnessing Macrophages for Vascularization in Tissue Engineering. *Ann. Biomed. Eng.* **2019**, *47*, 354−365.
(104) Lewis, C. E.; Harney, A. S.; Pollard, J. W. The Multifaceted Role of Perivascular Macrophages in Tumors. *Cancer Cell* **2016**, *30*, 18−25.
(105) Chillo, O.; Kleinert, E. C.; Lautz, T.; Lasch, M.; Pagel, J. I.; Heun, Y.; Troidl, K.; Fischer, S.; Caballero-Martinez, A.; Mauer, A.; Kurz, A. R. M.; Assmann, G.; Rehberg, M.; Kanse, S. M.; Nieswandt, B.; Walzog, B.; Reichel, C. A.; Mannell, H.; Preissner, K. T.; Deindl, E. Perivascular Mast Cells Govern Shear Stress-Induced Arteriogenesis by Orchestrating Leukocyte Function. *Cell Rep.* **2016**, *16*, 2197−2207.
(106) Nerem, R. M. Hemodynamics and the Vascular Endothelium. *J. Biomech. Eng.* **1993**, *115*, 510−514.
(107) Secomb, T. W. Hemodynamics. *Compr. Physiol.* **2016**, *6*, 975−1003.
(108) Choi, N. W.; Cabodi, M.; Held, B.; Gleghorn, J. P.; Bonassar, L. J.; Stroock, A. D. Microfluidic Scaffolds for Tissue Engineering. *Nat. Mater.* **2007**, *6*, 908−915.
(109) Dutta, D.; Heo, I.; Clevers, H. Disease Modeling in Stem Cell-Derived 3D Organoid Systems. *Trends Mol. Med.* **2017**, *23*, 393−410.
(110) Braet, F.; De Zanger, R.; Wisse, E. Drying Cells for SEM, AFM and TEM by Hexamethyldisilazane: A Study on Hepatic Endothelial Cells. *J. Microsc.* **1997**, *186*, 84−87.

DOI: 10.1021/acsnano.9b00686
ACS Nano 2019, 13, 7627−7643